UNIVERSITÀ
degli STUDI
di CATANIA

Dipartimento
di Fisica
e Astronomia
"Ettore Majorana"

PhD programme in physics

Vanessa Brio

Triple-GEM tracker and HCAL-J: two detectors for the study of Nucleon Form Factors at Jefferson Lab.

PhD thesis

Supervisors:
Chiar.ma Prof. C. Petta
Dr.ssa C.M. Sutera
Dr. E. Cisbani

Dottorato Di Ricerca in Fisica, Ciclo XXXIII

This work is dedicated to

Antonio and Salvatore

Contents

Introduction

In the experimental Hall A of the Thomas Jefferson National Laboratory (JLab, USA/VA) is underway the integration and installation of the different equipments which will constitute the experimental setup of the new SBS (Super BigBite Spectrometer) physics program, largely devoted to the measurements of the electromagnetic Nucleons Form Factors; the SBS program will start data taking in September 2021.

The present thesis work has focused on two key detectors of SBS: the GEM (Gas Electron Multiplier) based Front Tracker and the HCAL-J segmented hadron calorimeter. The latter is devoted mainly to provide the main trigger in the hadron arm, as well as the particles energy, the neutral pion identification and a course spatial correlation in high luminosity experiments; the former is an high spatial resolution charged particles tracker either in the electron or hadron arm, depending on the specific experiment of the SBS program.

The thesis activities have been carried on in the group of researchers, within the INFN-JLAB12 collaboration, composed by the Physics Depart-

ment of Catania, INFN of Catania, INFN of Bari, INFN of Genova and INFN of Rome, which has responsibilities in the development, construction, characterization and commissioning of both GEM Front Tracker and HCAL-J.

Microscopic simulations based on ANSYS mechanical modeler and the CERN-GARFIELD++ library have been implemented to better understand and characterize the GEM chambers performances. The relative complexity of the development of the charge avalanche in the GEM layers has been investigated on different mechanical models, approaches and initial conditions. Ultimately the simulations have been validated by test-beam data.

A central part of the thesis has involved the preparation, running and analysis of cosmic and LED based tests for the characterization and calibration of the HCAL-J sensors and electronics, primarily in terms of gains and time resolution of each module; the appropriate calibration of these parameters are fundamental for the operation of the whole calorimeter during the real experiment.

This thesis work is divided into five different chapters:

- in the First Chapter, the theoretical aspects of the Nucleon's Form Factors are described; furthermore the Jefferson Lab and its SBS experimental program for the study of the electromagnetic Form Factors is presented;

- In the Second Chapter, the Gas Electron Multiplier chambers will be introduced. Their geometry, the materials used for their construction, principle of operation, typical performance, and characteristics

chosen for their use within SBS are presented.

- In the Third Chapter, the Hadronic Calorimeter HCAL-J is introduced; its design and components will be described in details. The Electronics and the data acquisition system will also be discussed, together with some hints on the simulations of the Calorimeter;

- In the Fourth Chapter the two software used for the microscopic GEM simulations will be illustrated: ANSYS and GARFIELD++; in particular their general environments and the specific original implementation in the thesis will be described as well as the analysis of their behavior in different conditions. The results of the simulations will also be presented and compared with the data of the experimental tests on GEM modules performed at the Juelich Research Center in Germany, using a 2.8 GeV proton beam;

- In the Fifth and last Chapter, the tests carried out on the HCAL-J hadron calorimeter will be introduced; in particular, the results obtained from the first tests on a 4x4 matrix of modules and the increasingly accurate results regarding all the HCAL-J modules will be presented. The main tests will concern the calibration of all modules, the evaluation of the number of photoelectrons, and therefore their gain, and the timing resolution of the calorimeter.

Chapter 1

The Nucleon Form Factors

During the Twentieth century, the studies of numerous scientists have turned to nuclear matter and its constituents, Protons, Electrons and Neutrons.

The first systematic experiments to determine the internal structure of neutrons were made in the 1950s by Hofstadter and collaborators [1], at Stanford University in California, through numerous elastic diffusion experiments of electrons on protons. During the experiments, they used electrons with energies between 100 and 500 MeV in order to probe the charge distribution of the nuclei; the results of this investigation were: the direct confirmation of the no-pointlike nature of the proton and the measure of the radius of the latter.

Later in 1967 Friedman, Kendall and Taylor began performing a series of experiments at SLAC, with electrons up to 20 GeV, to study the structure and internal dynamics of the proton; these experiments they showed that the proton is composed "inside" of point-like particles, the Quarks. Since

then, numerous researchers have studied the structure of these elementary particles, confined within Hadrons, and their properties and strong nuclear forces that bind protons and neutrons.
The Nucleon Form Factors experimental studies do provide remarkable information on the structure of the nucleon; the Thomas Jefferson Laboratory is strongly involved in this research.

1.1 Theoretical Aspect

Let us consider the scattering process of an electron on a proton.
If we take the two particles as point-like, using the Born Approximation at the first order, we can describe the cross section of this process through the Rutherford cross section [2]:

$$\left(\frac{d\sigma}{d\Omega}\right)_{point} = \frac{\alpha^2}{4E^2 sin^4(\frac{\theta}{2})}, \tag{1.1}$$

where α is the fine structure constant, θ is the electron scattering angle and E is the energy of the electron.
When the target is not point-like but is extended, its magnetic moment and its spatial charge distribution must be considered; so it is possible to write the cross section of an electron on a nucleon in the following way:

$$\left(\frac{d\sigma}{d\Omega}\right)_{extended} = |F(q)|^2 \left(\frac{d\sigma}{d\Omega}\right)_{point}, \tag{1.2}$$

where q is the momentum transfer and F(q) is the Form Factor of the

nucleon.

In this approximation, we can describe the electromagnetic structure of the nucleon using the following Sachs form factors:

$$G_E(Q^2) = \int d^3\vec{r}\rho_E(\vec{r})e^{\left(\frac{i\vec{q}\cdot\vec{r}}{\hbar}\right)}, \tag{1.3}$$

$$G_M(Q^2) = \int d^3\vec{r}\rho_M(\vec{r})e^{\left(\frac{i\vec{q}\cdot\vec{r}}{\hbar}\right)}, \tag{1.4}$$

where $\hbar$ is the reduced Planck constant, r is the position vector, ρ_E and ρ_M are, respectively, the spatial charge distribution and the magnetic density of the nucleon, and $Q^2 = -q^2$ is the transferred four-momentum of the virtual photon. Fig. 1.1

If we consider a non-relativistic approximation, we can look at the electric and magnetic Form Factors of the Nucleons, such as the 3D Fourier transforms of the charge density and magnetization [2]; this means that, theoretically, it is possible to measure the distribution of electric charge inside the nucleon by doing the Fourier anti-transform of the Form Factor $F(q)$.

Experimentally, however, in the process of diffusion of electrons, the Nucleon Form Factors can be calculated using the following Rosenbluth Cross Section :

$$\left(\frac{d\sigma}{d\Omega}\right) = \left(\frac{d\sigma}{d\Omega}\right)_{Mott} \cdot \left[\frac{G_E^2(Q^2) + \tau G_M^2(Q^2)}{1+\tau} + 2\tau G_M^2(Q^2) tan^2\frac{\theta}{2}\right] \tag{1.5}$$

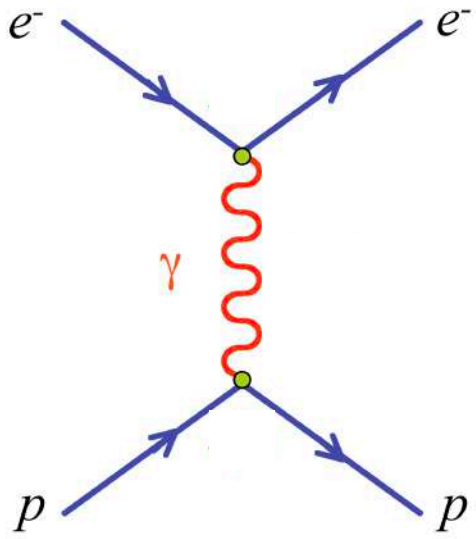

Figure 1.1: Feynman graph for electron proton scattering.

where θ is the scattering angle, c is the speed of light in vacuum, M is the target mass, $\tau = Q^2/4M^2c^2$ and

$$\left(\frac{d\sigma}{d\Omega}\right)_{Mott} = \frac{Z^2 \frac{e^4}{16\pi^2} cos^2\frac{\theta_e}{2}}{4p_0^2 sen^4\frac{\theta_e}{2}(1+\frac{2p_0}{M}sen^2\frac{\theta_e}{2})} \tag{1.6}$$

is the Mott cross-section, p_0 is the momentum of the incident electron and e is the charge of the electron.

Experimentally, to determine $G_E(Q^2$ and $G_M(Q^2$ [3], it is necessary measure the cross sections at pre-set values of Q^2, vary the energy of the beam and the angle of diffusion and divide the experimental cross sections for the corresponding Mott cross sections; in this way, if we graphed the results as a function of $tan^2(\frac{\theta}{2})$ we obtain the graph in Fig. 1.2, in which it is possible to see that, according to Rosenbluth's formula (1.5), the exper-

imental points all lie on a straight line slope we can obtain $G_M(Q^2$ while from the intercept on the y axis at x = 0 it is possible to extract $G_E(Q^2)$.

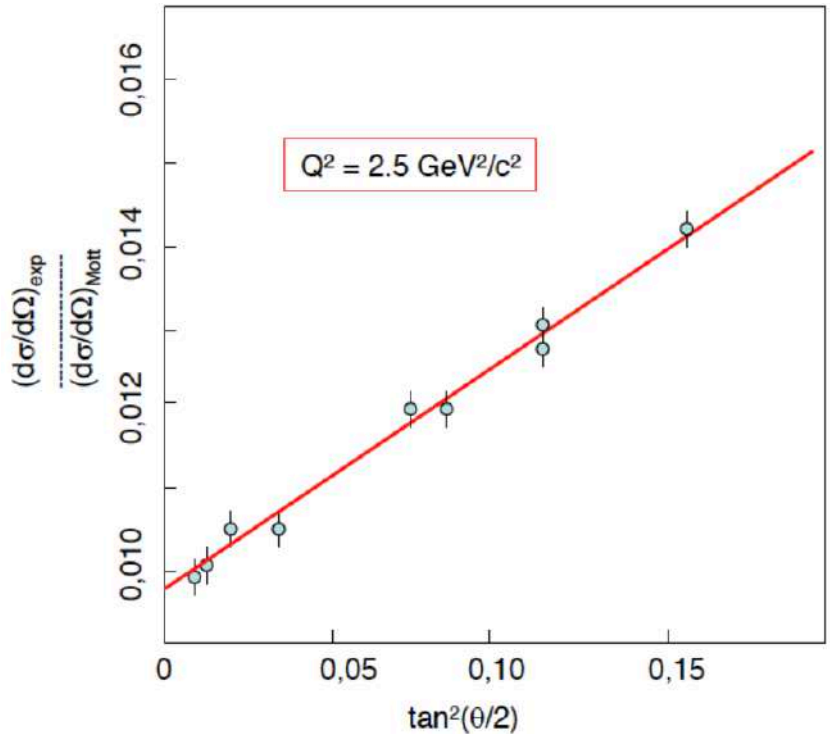

Figure 1.2: Line calculated through the ratio between the measured cross section and the Mott one, as a function of $tan^2(\frac{\theta}{2})$.

To establish the trend of the Nucleon Form Factors as a function of the quadrimpulse transferred, it is necessary to perform the measurement at different values of Q^2; what emerges is that protons and neutrons have a Form Factor that shows a similar trend, as a function of the quadrimpulse transferred, and which can be described by the same dipole fit [3]:

$$G_E^p(Q^2) = \frac{G_M^p(Q^2)}{\mu_p} = \frac{G_M^p(Q^2)}{\mu_n} = G^{dipole}(Q^2) = \left(1 + \frac{Q^2}{M_V^2}\right)^{-2} \quad (1.7)$$

where M_V is a constant $(0.71\frac{MeV}{c^2})$while μ_p and μ_n are respectively the anomalous magnetic moments of the proton and neutron. Such anomalous magnetic moments , derive from the calculation of the magnetic moments of nucleons at the limit of $Q^2 \to 0$, where $G_E(Q^2)$ coincides with the electric charge of the target nucleon while $G_M(Q^2)$ coincides with the moment magnetic of the target, i.e .:
$G_E^p(Q^2 = 0) = 1$,
$G_E^n(Q^2 = 0) = 0$,
$G_M^p(Q^2 = 0) = 2.79$,
$G_M^n(Q^2 = 0) = -1.91$.

Through numerous experimental measures, this trend has apparently been confirmed and also the fact that the relationships between the electric and magnetic Form Factor of the proton and between the electric Form Factor of the proton and the magnetic Form Factor of the neutron are practically constant, when the energies of the incident beam are not excessively high. Fig. 1.3
However, as early as 1957 [4], it was noted that the use of information of spin, through polarized beams and measurement of polarization transferred, would have allowed more accurate measurements, less dependent on Born-approximation, on which the Rosenbluth method is based.
If we have a polarized electron beam, and if we are able to measuring the polarization of the an elastically diffused nucleon, is possible to use the Recoil Polarization Method [5]; by this method it is possible to measure

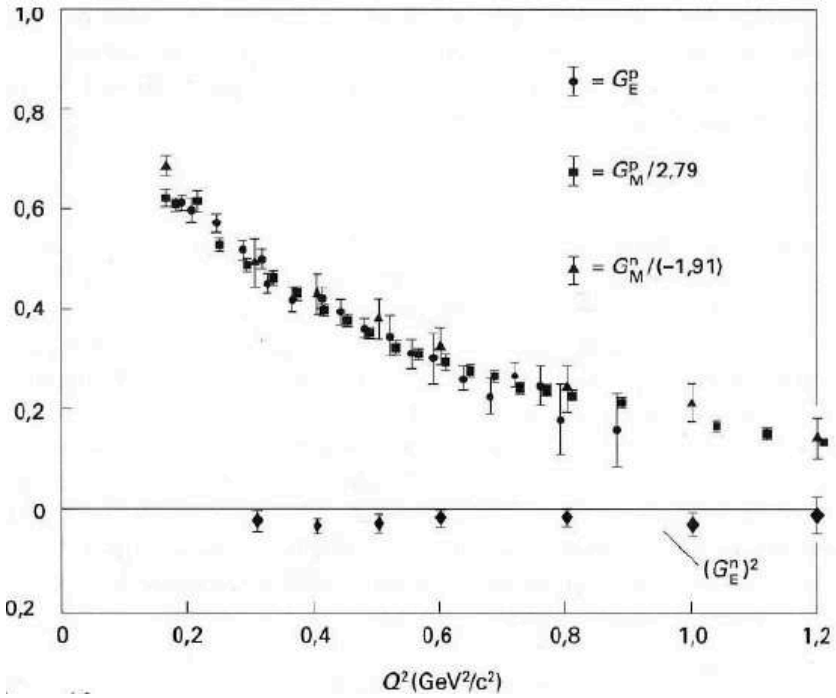

Figure 1.3: Experimental values of the Form Factors as a function of Q^2. It is possible to observe that these experimental values well approximate the dipole fit..

the two components, transverse P_t and longitudinal P_l, of the polarization of the recoil nucleon, one directly obtains the ratio between $G_E(Q^2)$ and $G_M(Q^2)$. The ratio is expressed by the relation: (1.8):

$$\frac{G_E(Q^2)}{G_M(Q^2)} = -\frac{P_t}{P_l}\frac{E_{beam}+E_e}{2M}tan\frac{\theta}{2} \tag{1.8}$$

where P_t and P_l are the two polarization's components, E_{beam} is the energy of the incident electron and E_e is the energy of the diffuse electron. The Recoil Polarization Method has been successfully adopted by JLAB starting from exp [5] [6], ; thanks to this method, it was possible to ob-

serve that in reality at high values of Q^2, the relationship between the electric and the magnetic Form Factors of the nucleon, does not follow the expected trend of the Rosenbluth's separation, but it decreases roughly linearly with the quadri-momentum transferred [6] as shown in Fig. 1.4

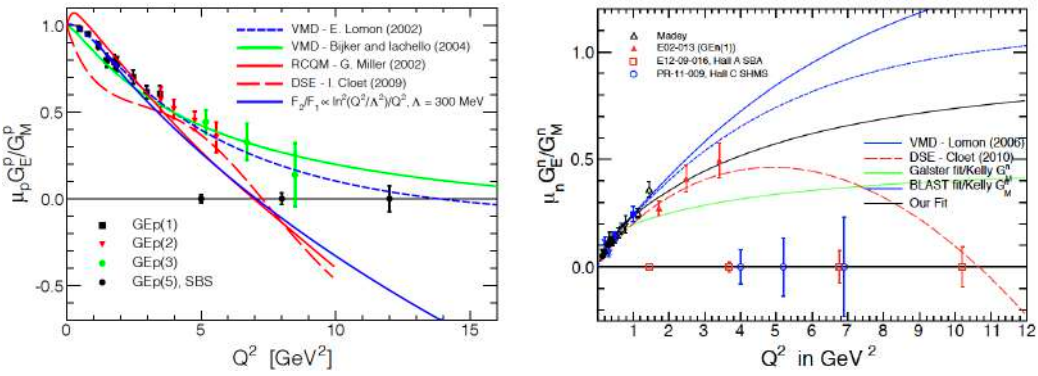

Figure 1.4: Experimental values of the proton (left) and neutron (right) Form Factors as a function of Q^2. It is possible to observe that the relationships between the Form Factors are not constant but decrease as the quadri-momentum transferred increases.

The most accredited hypothesis that explains the discrepancy between the Rosenbluth's separation method and the Recoil Polarization Method is that the Rosenbluth method does not take into account the effect of the exchange of two photons in the electron-proton scattering process.
On the other hand, the decrease in the ratio of the proton Form Factors at high Q^2 values, requires a review of the models on the nucleon structure[7]. A recent study [8] on the contributions of different flavor of the quarks, to the Form Factor seems to indicate the presence of a diquark structure inside the proton, which, moreover, could be linked to the point

in Q^2 of zero-crossing the 0 of the ratio of the proton Form Factors [9]
The discrepancy, at high Q^2, in the results of Form Factors measurements, it occurs, in another form, also for $Q^2 \to 0$, where the Form Factors can be used for the estimation of the nucleon radius. Very advanced recent measurements of the proton radius, by spectroscopies techniques [10], showed a discrepancy of at least 6 sigma with respect to measurements based on form factors; this originated the so-called "Proton radius crisis" showing the need to deepen the Form Factor studies and measurements. Today high values of Q^2 can be achieved thanks to the CEBAF (Continuous Electron Beam Accelerator) upgrade up to 12 GeV at JLAB, and, thanks to the new experiments, we could better understanding the nucleon Form Factors and the interaction mechanisms between electrons and nucleons.

1.2 The New SuperBigBite Spectrometer at Jefferson Laboratory

The Thomas Jefferson National Accelerator Facility, commonly called Jefferson Lab or JLab [11], is an important American laboratory, located in Virginia, whose main purpose is to investigate the fundamental nature of nuclear matter, or the way in which the nucleons are combine each other to form the atomic nucleus and what are the forces that bind them together.
At JLAB there are 4 different experimental rooms, called HALL A,B,C and D that share the same electron accelerator called CEBAF; this accelerator

produces a continuous high intensity electron beam, so a current that can reach up to 100 μA, using superconducting radio frequency technology (SRF) [12] [13] and generating an electron beam with an energy that can reach, thanks to a recent upgrade [14], up to 12 GeV and it is capable of delivering beams of up to 85 μA, which corresponds in some experiments to luminosities up to $10^{39} electron/s - nucleon/cm^2$.

In each experimental hall, there are different detection systems, that are under construction or already available, for the extensive and diversified experimental laboratory program. For the Hall A, a new Spectrometer, called Super BigBite (SBS),is under finalization and will be used, in different configurations, for a lot of experiments to study the Nucleon Form Factors. The main features of SBS are: large solid angle, large momentum acceptance (from 2 GeV/c), high luminosity capability, small scattering angle capability (down to 3.5 deg), very good angular resolution ($\sigma_\theta[mrad] = 0.14 + 1.3/p[GeV/c]$), good momentum resolution ($\sigma_y \approx 1 - 2mm$) and a good momentum resolution ($\sigma_p/p = 0.0029 + 0.0003 \times p[GeV/c]$) [15]. The SBS spectrometer, will also provide a solid angle of 70 msr and a very large luminosity and will consists of two arms, one to detect the electrons and the other to detect the hadrons, that will be described in the next sections.

1.2.1 Electron Arm

The electron Arm of SBS [16], is useful to detect the electrons; this arm was composed, in the original configuration, from the existing Big Bite Spectrometer, Fig.1.5 that included a magnet, a tracker system based on

Multi Wire Drift Chambers (MWDCs), a gas Cherenkov counter (GRINCH), and a double-layer lead glass shower counter; the Big Bite acceptance is about 64 mrs and the magnet can reach a maximum integrated field of 1.2 $T \cdot m$.

Now, The original 3 MWDC layers have been replaced by 4 GEM front layers before the GRINCH in the first experiment of the SBS program and one layer after it. The 4 GEM in the front of GRINCH are made of two chambers which will be described in the next chapter and two GEM with u/v strip orientation (+/-60 deg relative to the horizontal axis); more on the GEM in the following paragraphs and chapters.

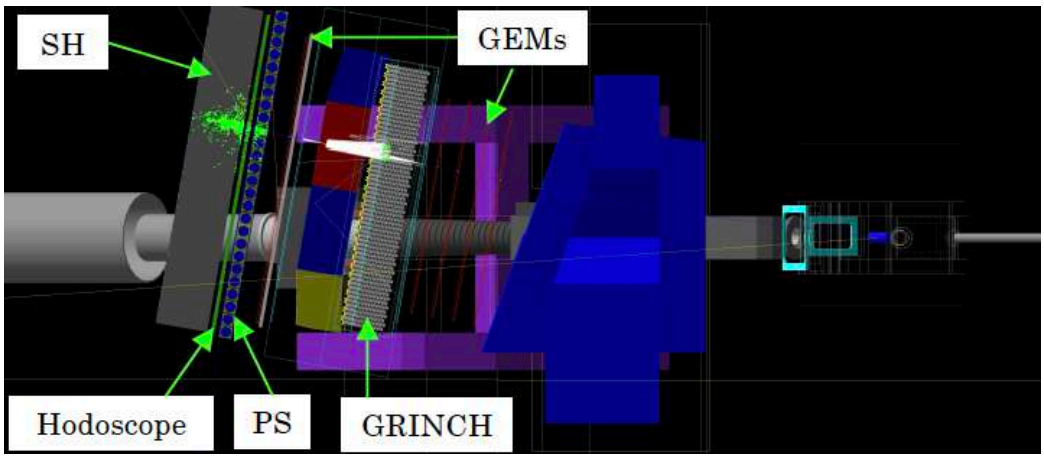

Figure 1.5: Big Bite configuration and its components.

The GRINCH will be use, together with the large double-layer shower detector, as BigBite trigger system, in particular to distinguish good electron events from pion and electromagnetic contamination.

The Timing from BigBite is provided by a plastic scintillator hodoscope

that consists in an array of plastic scintillator bars arranged in a vertical stack sandwiched between the pre-shower and shower lead glass arrays. Each bar is read out by two 29 mm PMT and position independent timing is given by the mean time from the two PMT. Time difference gives the horizontal hit position. BB-hodo covers the full range of coordinates of the lead glass arrays [17].

The Big Bite's electromagnetic calorimeter is a segmented lead glass calorimeter, divided in two parts knows was the preshower and shower, with a plastic scintillator plane between the showers. The preshower, consists of a 2×27 plane of 37 cm ×8.5 cm blocks. The shower, about 1 m behind the first GEM chamber, consists of an 7 × 27 array of 8.5 cm × 8.5 cm blocks. The preshower signal can be also used to provide an additional method of pion rejection [18].

1.2.2 Hadron Arm

The hadron arm of SBS, mainly detect protons and pions. The components of the hadronic arm can be arranged in different configurations, depending on the experiment for which they are to be used. The most complete configuration is that of the G_E^p experiment, which we will talk about in the next section.

The components of SBS are:

The Dipole Magnet 48D48

The magnet, Fig. 1.6, about 100 tons total, is useful to deflect the products of the reaction and direct them towards the detection system; it could reach $3T \cdot m$ field integral when the current is about $4kA$. This magnet

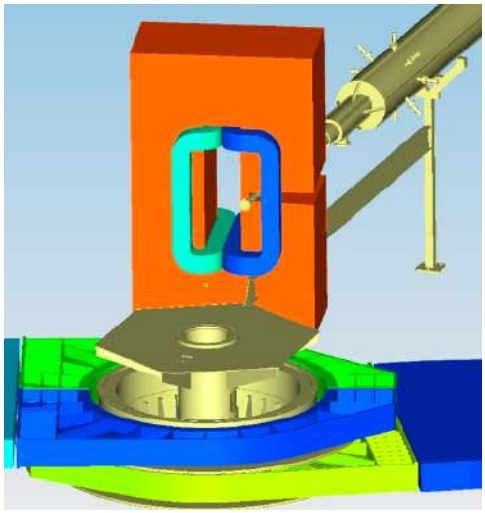

Figure 1.6: 48D48 Dipole Magnet

consists of five iron slabs and a cut in yoke that permits to operate at small angles; the vertical aperture well matched to electron arm and it is appropriate for $\Delta Q^2/Q^2 = 0.1$. The dipole also provides an adequate momentum resolution, about 1%.

The GEMs Trackers

A series of Gas Electron Multiplier will be used for the different Form Factor Experiments; this technology, that we will describe in the next chapter, is based on gas avalanche multiplication in small holes drilled in a copper and kapton bun. The main features of GEM foil are: high gain (using several GEM foil), stability in operation, high rate capability (up to 100 MHz per cm^2) and an excellent position resolution (about 70 μm).

The Polarimeter

The polarimeter, that consists of two trackers each preceded by a CH_2 analyzer, will be used to measure the components of the proton spin po-

larization, in G_E^p experiment. In fact, it is known that to use the Recoil Polarization Method, it is essential to measure the ratio between the two components, longitudinal and transverse, of the recoil proton. In particular, the first polarimeter determine the proton polarization components measuring the azimuthal asymmetry of the secondary trajectory with respect to the initial one, while the second polarimeter analyze the polarization of the protons not scattered in the first polarimeter or measuring for a second time the polarization of the scattered protons [15].

The Hadron Calorimeter HCAL-J

The Hadron calorimeter HCAL-J, that will be detailed in the chapter 4, will be useful to measure the energy of scattered nucleons and distinguish protons to neutrons. HCAL-J is a sampling calorimeter with a good position resolution and will be positioned in a rollable stand to permit to move the calorimeter according to the different experiments. The first Form Factor experiment that will use this calorimeter, is G_M^n, that should start at the end of the 2021, and that will be described in the next section.

1.3 SBS Experimental Program At JLAB

The SBS program, for the HallA, will measure the nucleon Form Factors, G_M^n, G_E^n, G_E^p at significantly higher Q^2 value than has been done before. Some of the Form Factor experiments are briefly listed below.

1.3.1 The GMn experiment

The GMn experiment, approved in 2008, is an HALL A experiment to measure the magnetic form factor of the neutron, directing the electron beam at a target of non-polarized liquid deuterium [19]; in particular, the magnetic form factor of the neutron, will be measured comparing the non-polarized elastic cross section of the two different ones processes $d(e,e'p)$ and $d(e,e'n)$.
This experiment will be performed at precise values Q^2 ranging from 3.5 to 18 GeV^2, and will use the "ratio method" to determine G_M^n from quasi-elastic electron scattering on the deuteron; during the experiment, the BigBite spectrometer and the Super Bigbite magnet will be used in order to obtain an excellent separation between recoil protons and recoil neutrons.
For the experiment the SBS configuration in Fig. 1.7 will be used.

1.3.2 The GEn experiment

The GEn experiment was approved in 2009 at the JLab [18], to study, at high values of Q^2, the electric form factors of the neutron; in particular, we can measure, at $Q^2 = 5.0, 6.8, and 10.2 GeV^2$ the double-spin-asymmetry,in the reaction $^3He(\vec{e},e'n)pp$, in a quasi-elastic collision between a polarized electron beam and a target of ^3He also polarized.
To measure the electromagnetic form factor ratio of the neutron will be used the same SBS configuration of the G_M^n experiment Fig. 1.7; during the experiment, the electrons will be detected in the BigBite spectrometer

with a GEM tracker and the neutrons in an array of scintillators.

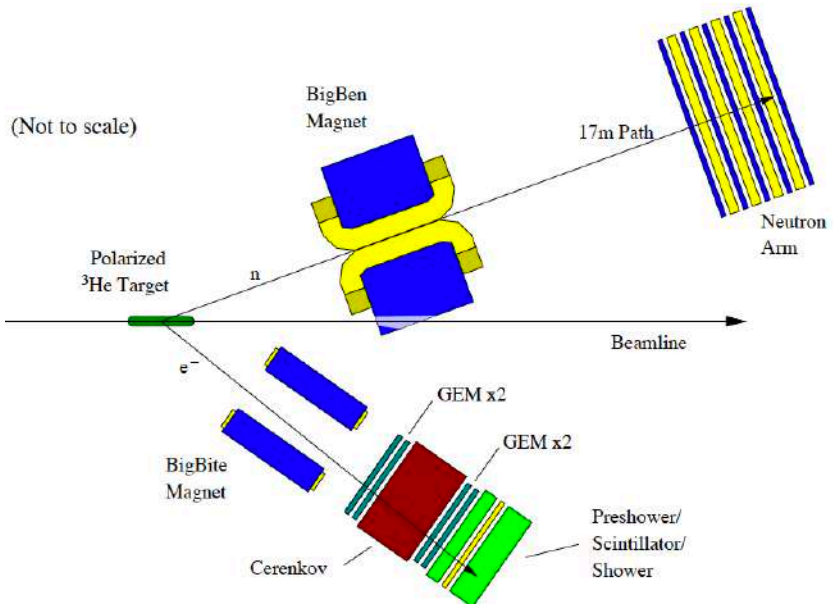

Figure 1.7: SBS configuration for G_E^n experiment.

1.3.3 The $GEp5$ experiment

The $GEp5$ experiment was approved in 2008, and it permits to measure electric over magnetic Form Factor ratio of the proton, using the Recoil Polarization Method [20].

For this experiment, the electron beam will pass through a 40 cm long LH2 target and the electron will be detected in the electromagnetic calorimeter BigCal; for the proton arm, the configuration is shown in figure 1.8 and the layout consists of a magnet, a system of GEM tracker and CH2 polarimeters and an hadron calorimeter HCAL-J.

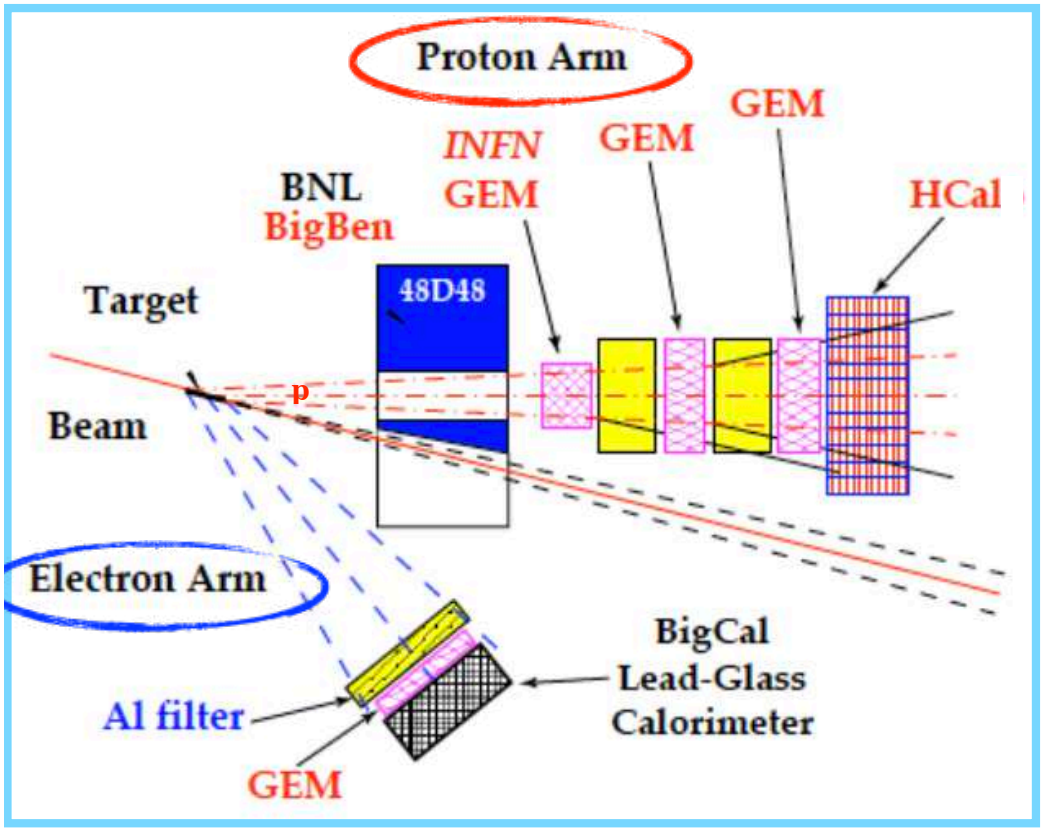

Figure 1.8: SBS configuration for G_E^p experiment.

Chapter 2

Gas Electron Multiplier: Front Tracker For SBS

The GEM trackers (Gas Electron Multiplier) are gaseous detectors and fall into the category of micro-pattern detectors; this technology was introduced in 1997 by Fabio Sauli, at CERN [21] and it was initially developed for high-energy particle physics studies. In a gaseous detector, when a charged particle passes through a gas, it loses its energy creating electron-ion pairs; these particles, if accelerated by an appropriate electric field, are pushed towards the electrodes and then collected. The GEM tracker works in a proportional regime so the electrons produced during the first ionization can acquire, between one collision and another, sufficient energy to ionize again and create an avalanche.

As we will see in this chapter, the GEM foil are very performing in terms of radiation robustness, they have an excellent spatial resolution and a good time resolution, and their costs are lower than other detectors (Si

for example).

2.1 Single GEM foil

A GEM foil consists in a thin layer of Kapton (a dielectric material), in particular 50 μm, coated on both sides by a very thin layer of copper with a thickness of 5 μm. In this layered structure, there are a lot of holes arranged so that their centers are always 140 nm apart, in a triangular pattern. [22]. The geometry of the holes is typically biconical; the outside diameter of the holes is 70 μm, while the internal diameter is 50 μm Fig.2.1. These holes practically constitute the active part of the detector, ie the region in which the multiplication of electrons takes place.

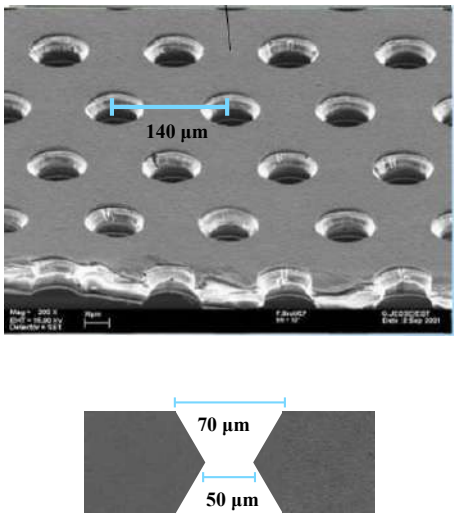

Figure 2.1: Above, electron microscope picture of a section of typical GEM and its holes; below, a biconical hole.

The GEM foil is placed between a drift plane and a readout plane, Fig. 2.2; if we apply an appropriate potential difference to the copper ends, usually between 300 and 500 Volts, an high electric field is generated which directs the electrons created by ionization towards the biconical holes. Inside the hole, the electrons are accelerated by the electric field and acquire energy to create a multiplication avalanche, with a nominal gain of about 20 electrons for each electron that enters the hole. In particular, the potential difference at the ends of the foil, directs the electrons, which meanwhile they multiplied, towards the readout plane, while conveying the ions towards the drift plane.

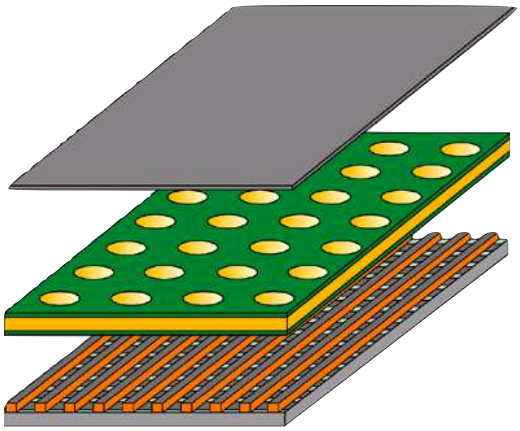

Figure 2.2: Single GEM foil between drift and readout planes.

When the voltage is applied in the drift plane and in readout plane, different electric fields are created, Fig. 2.3, and in particular [23]:

- Drift Field: between the drift plane and the upper side of the GEM foil; it's know, from experimental evidence, that the intensity that allows the greatest number of electrons to direct itself towards the

holes of the GEM is between 1 and $3kV/cm$.

- Induction Field: between the lower side of the GEM foil and the readout plane, that usually it's maintained at 0 Volt; a too low value of this field, would not allow to collect the charge produced, while a too high value could generate multiplication effects with discharges fenomena in proximity of the readout plane border.

- Holes Field: it is the very intense field that is established inside the holes, that is between the two metal faces of the GEM foil. A much higher intensity of this field, would allow a greater flux of electrons inside the holes but it could happen that many secondary electrons are blocked from the bottom of the GEM.

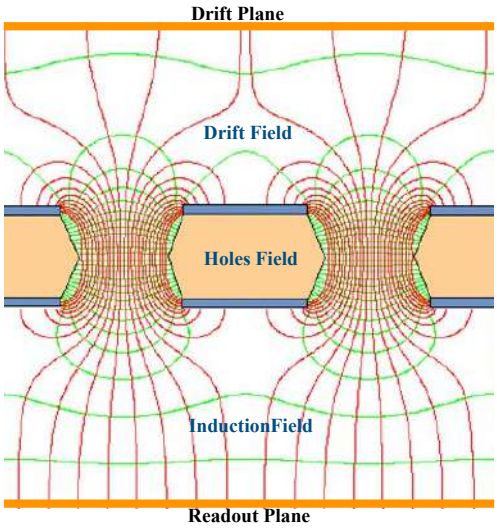

Figure 2.3: Configuration of the fields that are created within a GEM foil.

In general, the collection time is very fast, about 100 ns, with rise signal (useful for eventual timing information) of the order of some ns.

As for gas, actually many types of gas can be used, but the choice are often the noble gases for the following reasons:

- Noble gases are not electronegative, ie they do not have the "capacity" to capture electrons;
- they have a reasonably low effective ionization potential;
- it is not necessary to generate a high electric field to start the ionization and charge multiplication process;
- generally they have relatively low costs.

Usually the most used gas is Argon, because it has a low value of ionization energy, is readily available and its costs are low. What happens is that, UV photons can be emitted by the de-excitation of the molecule so there is the necessity to use some gases called quenchers that absorb such photons so as to "not disturb" the signal coming from the electrons; the most widely used polyatomic quencher gases are CO2, CH4 and other hydrocarbons.
For these reasons, in a GEM chamber the gas is composed by a mixture of gases, that is composed largely of Argon and a small part of quenching gas.
As already mentioned, the GEM tracker present several advantages over traditional gas detectors. Thanks to them "layered" structure the main processes occurring in the chamber: ionization, multiplication and collections are largely independent; in fact the multiplication of electrons occurs near and inside the holes that act as a multiplication channels,

while the collection part takes place in the anode which is like a "separate structure". Furthermore, this modular structure, makes the GEM trackers a very good detectors to obtain a large gain in terms of the amount of electrons in the final state and also very robust both from the point of view of discharges than from that of aging, which depends from the materials used in the construction and from the composition of gas [23].
Another advantage of the GEM trackers is their flexible geometry, or the fact that, based on the experiment in which they must be used, these trackers can be easily configured and optimized in terms of shape and diameter of the holes, distance between the latter, thickness of various materials etc. In addition, the GEM trackers are relatively unexpensive and they allow to obtain a high gain, as we will see later, without use too high potential differences between cathode and anode. In addition, the GEM trackers are very robust and resistant to the radiation, they allow to obtain a good spatial resolution, about 70 - 100 μm, and it is possible to reduce the probability of discharges using many GEM foils placed in cascade (like we will see in the Triple GEM configuration section); that means that by using more amplification steps we could still obtain a very good total gain without using a very high voltage value [24].
Among the disadvantages of GEMs trackers, there is the "charging-up" phenomenon, which consists in the impossibility of the insulating layer in the readout plane, to neutralize the charges present in it with the result of an alteration of the field and so problems of accuracy and efficiency. Also if you use very high potential difference, the “streamer" phenomenon could occur, and so the charge collected on the readout plane is no longer

proportional to that produced during the ionizations but has a higher value that brings the system into an uncontrolled regime in which discharges are more frequent.

We mentioned earlier that GEM foils can have different geometric and structural configurations , based on their use in several experiments, so different geometrical parameters impact on [21]:

- collection efficiency, that we will deepen later, that is affected by the pitch between the holes;
- charging-up phenomenon, that depends from the shape of the holes;
- the gain, that is affected by the holes diameter; it has been seen that however for diameters smaller than $70\mu m$ there is a saturation of the gain, in Fig.2.4.

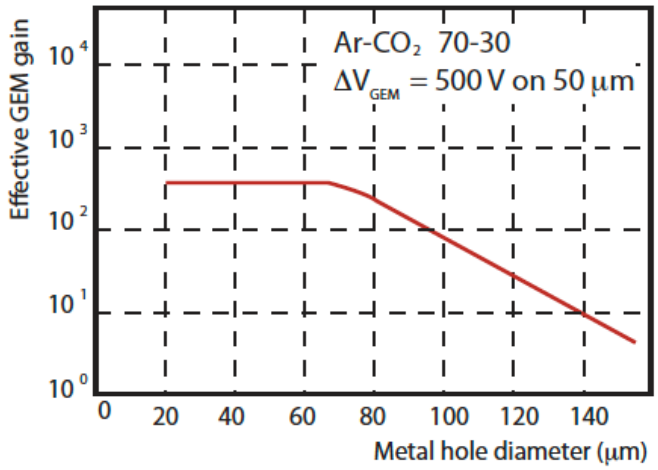

Figure 2.4: Gain of a GEM foil, in an Ar-CO2 gas mixture, in function to the diameter of the holes.

2.1.1 Single GEM gain

As mentioned above, the high voltage to apply to a GEM foil must be chosen to create a stable electric field that allows to obtain an adequate gain in terms of collected charge, that is signal on the readout plane, and at the same time not excessively high to prevent discharges.
Electrons acquire kinetic energy, under the action of the electric field and create an avalanche multiplication; let n_0 be the number of initial electrons at the coordinate point x = 0, the number of electrons at the point $x \neq 0$ is given by the following relation[25]:

$$n = n_0 e^{\alpha x} \tag{2.1}$$

where α is the Towsend coefficient, that represents the number of ionizations per unit of length. This Townsend coefficient depends from the electric field E, from the type of gas mixture and the gas pressure p (see table below) so, if we indicate with A and B the two parameters that enclose the dependence on the type of gas, we can write:

$$\alpha = Ape^{-B\frac{p}{E}} \tag{2.2}$$

We can define Intrinsic Gain as:

$$G = \frac{n}{n_0} = e^{\alpha x}. \tag{2.3}$$

The intrinsic gain of a single GEM foil can reach values up to 10^3 , but as we will discuss, not all the electrons of the avalanche reach the readout plane, therefore the effective gain is less than this value.

Gas	A $[cm^{-1}Torr]$	B $[cm^{-1}Torr]$
He	3	34
Ar	14	180
Xe	26	350
CO_2	20	466

Table 2.1: A and B coefficient values for different gases.

To study the gain that is possible to obtain using a single GEM foil, it is appropriate to introduce two new factors, the collection efficiency and the extraction coefficient [23]:

- The collection efficiency ϵ_{inf}, indicates the ratio between the number of electrons entering the hole of the GEM foil and the number of electrons produced in the drift gap, which is the region between the drift and the top face of the GEM. Many electrons, due to diffusion phenomena, do not pass through the holes but remain "attached" to the top of the GEM foil face;

- The extraction coefficient ϵ_{extr} indicates the ratio of the number of electrons that are extracted from the holes and the number of electrons produced from the avalanche inside the holes.

So ultimately, the factors that affect the collection efficiency and the extraction coefficient and therefore the gains are:

- the intensity of the drift fields and the induction field;

- the thickness of drift region and induction region;

- the applied potential between drift and readout plane;
- the applied potential between the two GEM faces;
- the width and height of the holes.

2.2 Triple GEM Chamber

Three GEM foils placed in cascade between a drift and a readout plane, constitute a triple GEM tracker, Fig. 2.5.

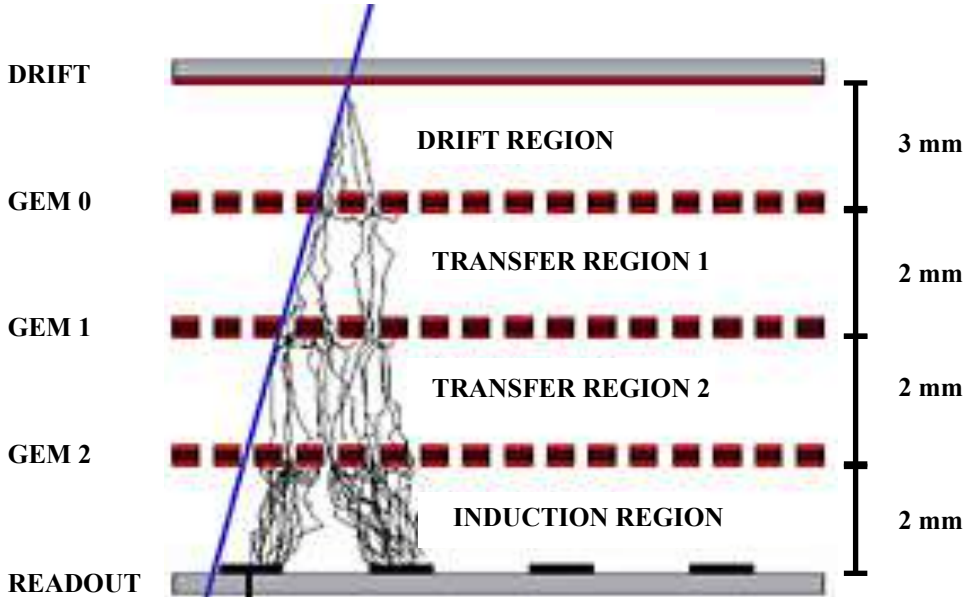

Figure 2.5: Configuration of a Triple GEM detector.

The operating principle of the triple GEM chamber is identical to that of the single GEM foil and exploit the above-mentioned independence of the different processes occurring in a GEM chamber; in fact the drift region

and the induction one, have the same "task" as the relative ones regions previously defined in the single GEM foil, while the intermediate zones, between one GEM and another, are called transfer regions. These regions have the dual task of acting as a drift region for the following GEM and as induction region for the previous GEM; this means that the value of the electric field in the transfer region it must be such as to allow a good extraction of the electrons from the upper GEM and an efficient insertion of the electrons into the holes of the next GEM (the optimal value is about 3-5 kV / cm).

As in the case of the single GEM foil, also for the triple GEM chamber the dimensions between the various regions are very important in order to get a high gain; for the drift and induction regions it is true what has been said for the single GEM foil, but for the transfer regions a different reasoning needs to be made.

If an electron is produced in the first transfer region, it undergoes only two stages of multiplication and consequently the induced signal from these electrons have a smaller amplitude and an anticipated time compared to those produced in the drift region; this phenomenon is said bi-GEM and the result is an "expanded" temporal distribution of the events. In the second transfer region, the bi-GEM event is negligible but the discharges phenomenon could be a problem; in fact in the third multiplication stage, the number of pairs is big and could be create the streamer phenomenon resulting in a discharge phenomenon. For these reasons the optimal thickness of the transition zones is about 1 mm [26]

The intrinsic gain that can be obtained using a triple GEM is given by the

following formula:

$$G \propto e^{<\alpha>\sum(V_{tot})} \tag{2.4}$$

where V_{tot} is the sum of all the applied voltage in the triple GEM chamber. Obviously, as in the case of the single GEM foil, the effective gain of the Triple GEM is lower than the intrinsic one and reaches values equal to 10^5.

The reasons why the triple GEM configuration is often used are:

- amplification occurs in successive stages;
- high gain values are obtained combining lower single GEM gains reducing discharge phenomena;
- lower ion and photon feedbacks to the cathode.

2.3 Readout Plane Geometry

The charge avalanche generated along the particle track traversing the GEM layers, can be collected on a segmented readout surface. The effective independence of the multiplication phase (in the GEM foils) from the drift of the charge and its collection one, the readout geometry can vary depending on the specific needs. The readout plane is usually made up of a Kapton foil with copper on one side, with a geometry that can assume two main class of configurations: strip or pad.

The readout can contain multiple kapton-copper layers where, for example, the pad on the top layer are connected to strips on the bottom layer which transfer the pads collected charge toward the readout electronics.

In the strip configuration (used in SBS) the readout has two strip layers (5 μm copper + 50 μm kapton), as in Fig. 2.6, with strip oriented at either 90 degrees (X/Y) or 60/30 degree (U/V), allowing a correlated 2-dimensional readout. In both configurations, the strips have a typical distance of 400 μm [25] (essentially defined by the width of the electron avalanche) and therefore a spatial resolution better then 100 μm).

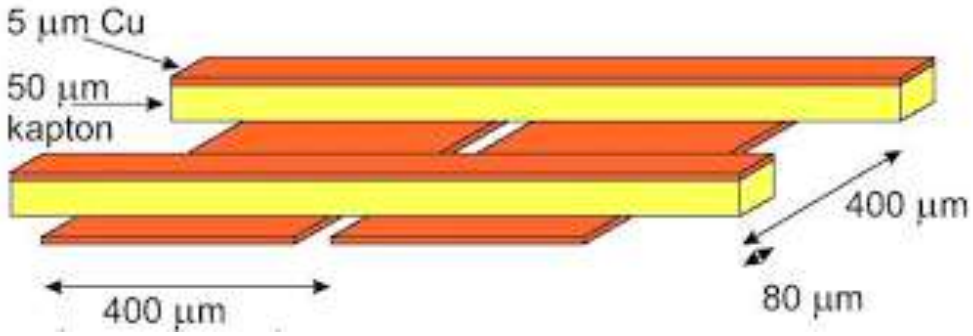

Figure 2.6: Strip Readout for SBS configuration.

2.4 Front Tracker for SBS

In the configuration of the most demanding experiment of the SBS physics program (GEp5), the Front Tracker will be composed of six GEM chambers (layers), alternating X/Y and U/V strip readout layers, with an active transverse area of $40x150cm^2$; each X/Y layer is made of three independent triple GEM modules of $40x150cm^2$, Fig. 2.7, [22], while the U/V layer is made of a tall single triple GEM module.

These GEM layers will be reconfigured on the electron and/or hadron

arm for the other SBS experiments, depending on the specific experimental requirements. .

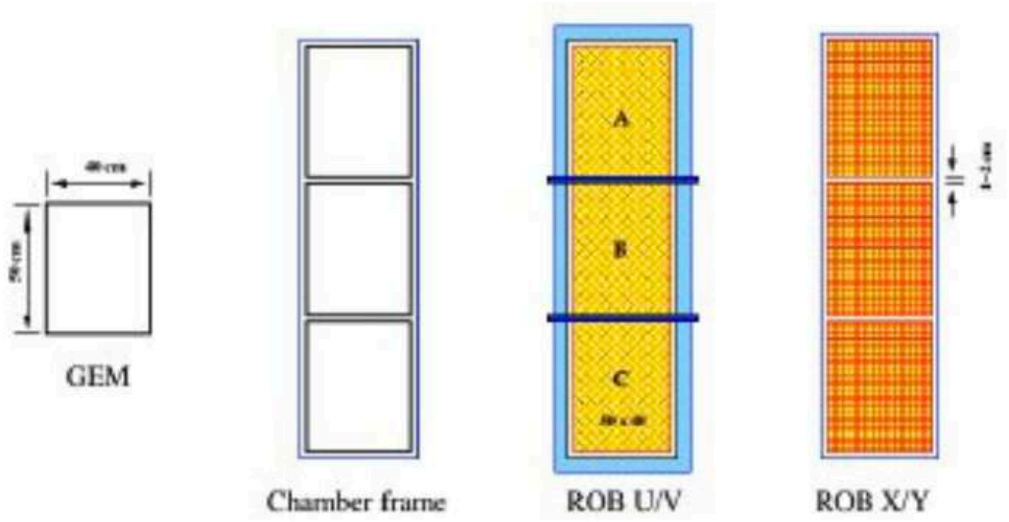

Figure 2.7: One X/Y SBS tracker layer with the three independent GEM modules; visible the readout electronics all around the modules and the relative cabling.

The front-end readout electronics is based on the APV25 chip, developed by the Imperial College London, [27]. Each APV25 chip essentially amplifies and continuously samples the signals of 128 strips; the analog multiplexed output samples are readout and digitized by VME-VXS modules (Multi Purpose Digitizer) specifically developed by INFN [28] which can then transfer the digital data either over the VME-VXS bus or an optical link to the JLab event builder system.

The front-end cards used are 18 per module and are distributed along the four sides of the frame. Each front-end card (FEC) contains an APV25

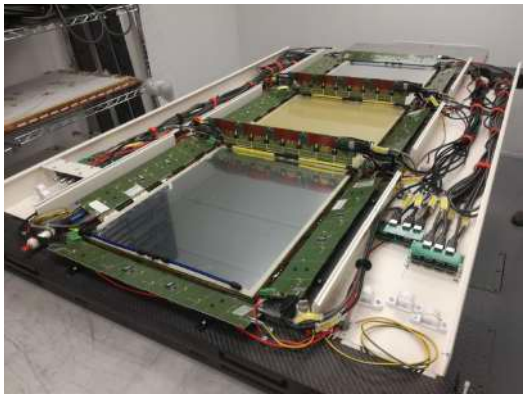

Figure 2.8: X/Y strip readout in the SBS configuration.

(Analogue Pipeline Voltage) chip, developed by Imperial College London, and that APV25 chip is an analogue Application Specific Integral Circuit (ASIC) pipeline with a serial multiplexed output. It was designed to tolerate high amounts of incident radiation [29].

Chapter 3

HCAL-J: Hadronic Calorimeter For SBS

In the hadron arm of the SBS spectrometer, an hadron calorimeter is provided; this calorimeter will be placed in the last part of this arm, to evaluate the energy of protons and neutrons in GMn experiment, the neutrons in GEn and the recoiling protons in GEp5 experiments [30].
In the course of this chapter, we will describe the main features and requirements of this detector, which are useful for carrying out the Form Factors experiments for the HALL A.

3.1 Calorimeter Design And Requirements

HCAL-J is a sampling calorimeter with a modular structure, whose design is based on COMPASS HCAL1 calorimeter [31]; this calorimeter was useful to detect at CERN hadrons up to 100 GeV.

HCAL-J will be the last components of the SBS hadron arm and will be used for the first time in GMn experiment, in September 2021.
The main components of HCAL-J are [32]:

- The modules;
- the front end electronics;
- the internal LED system;
- the dry air supply;
- the high voltage system;
- the data acquisition electronics.

and the most important requirements, for the Form Factors experiments are [30]:

- matching acceptance with SBS magnet/polarimeter;
- linear energy response;
- good energy resolution;
- 95% efficiency with trigger threshold at 25% mean signal;
- spatial resolution $\sim$ 5 cm rms;
- time resolution $\sim$ 1.0 ns rms (Goal: 0.5 ns);
- angular resolution 5 mrad.

HCAL-J has an active area of 288 modules arranged in a matrix of 12x24 modules each with 15x15 cm^2 surface; each module is composed of 40 alternating layers of iron, in which the hadron shower forms, and 40 plastic scintillators sampling its energy [30]. In total the calorimeter has an area of 360 cm in height, 180 cm in widht and 100 cm in thickness Fig.3.1, with a total weight of about 40 tons.

At the moment, HCAL-J is divided into four sub-assemblies and will

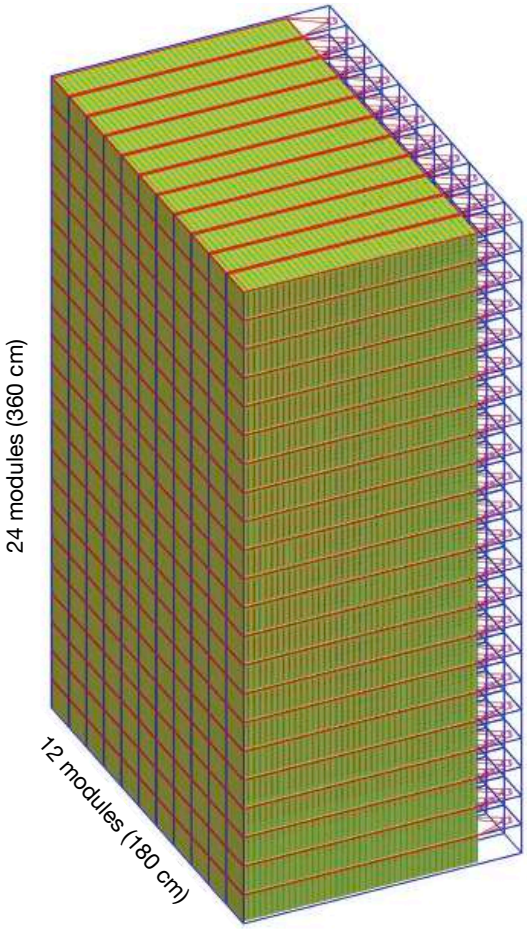

Figure 3.1: HCAL-J calorimeter design.

be placed in a Rollable stand to move the gantry and HCAL-J together without need to disconnect cables.

A wavelength shifter (WLS, St.Gobain BC-484, with a decay time about 3 ns) is placed in the middle of each module Fig. 3.2, to have a better efficiency and uniformity in the light collection; in particulare for HCLA-J a very fast WLS, paired to extruded plastic scintillators (PPO only, 2,5-Diphenyloxazole), made by Fermilab, is used.

Figure 3.2: Configuration of each HCAL-J module with WLS and light guide.

The WLS is connected to a photomultiplier (PMT), in order to collect the light from the scintillating material and convert it into an electric signal related to the energy of the incident particle [30] Fig. 3.3; in this calorimeter there are two different types of photomultipliers: 96 LAB tubes (21-pin, 8-stageXP2282) and 192 CMU tubes (19-pin, 12-stage XP2262). HCAL-J also has a series of 6 LEDs that can illuminate each PMT, Fig.3.4; Each subsequent LED lights up twice as much as the previous one.

The HCAL-J collaboration group is formed by JLab, Carnegie Mellon University and INFN of Catania section; in particular, the Catania group:

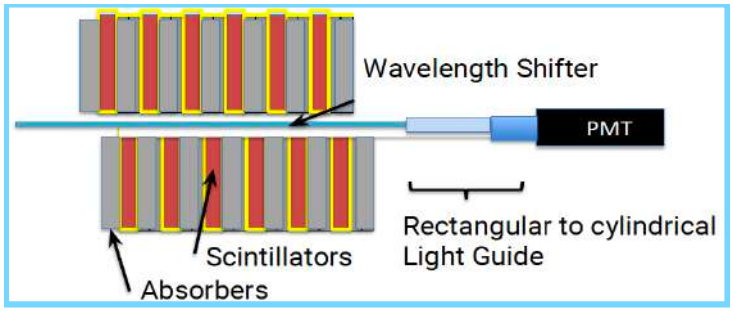

Figure 3.3: Complete configuration of each HCAL-J module.

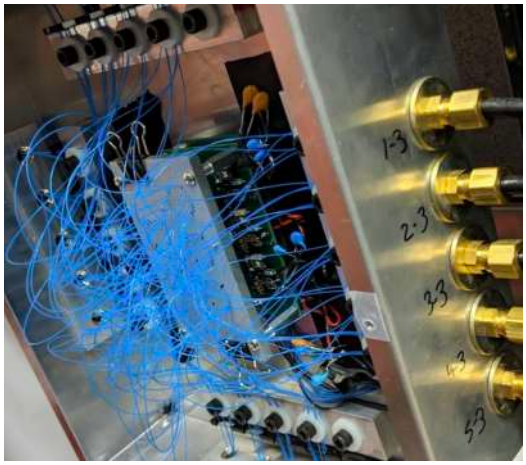

Figure 3.4: LED configuration on HCAL-J.

- took part to the development of the HCAL-J concept in the framework of the Consortium CMU/INFN&UniCT/JLab (working group of the Hall A Collaboration);
- organised the construction procuring the WLS, the light guides and the iron absorbers;
- was involved in PMT's construction;
- was involved in the procurement and setup of a part of the electron-

ics;

- completed the cable gantry and rollable stand;
- test and data analysis.

3.2 Electronics And Data Acquisition System

As for HCAL-J electronics, this will be distributed in five racks; three of these racks are part of the front end electronics (RR1, RR2, and RR3) Fig. 3.5, while the other two racks are the DAQ electronics These racks are grouped into the front-end electronics (RR4 and RR5), Fig. 3.6.
The front-end electronics will be located behind HCAL-J, when the calorimeter will be moved in the experimental Hall A, and the DAQ electronics will be located in a shielded electronics hut upstream of the target to protect the electronics from radiation damage; the front-end electronics are connected to the DAQ electronics via 100 meter long BNC cables.

3.2.1 Front-end Electronics

The front-end electronics [33] contains 18 Phillips Scientific 776 16 channel amplifiers which amplify the detector signals from the PMTs by a factor of ten; nine amplifiers are powered in rack RR1, and the other nine in rack RR3. 18 Phillips Scientific 706 16 channel discriminators are situated in rack RR2; these discriminators are set with a thresholds, of 11 mV, and produce a NIM logic signal to be sent to the DAQ for TDC timing measurements. The signal enters the front-end through the amplifiers at

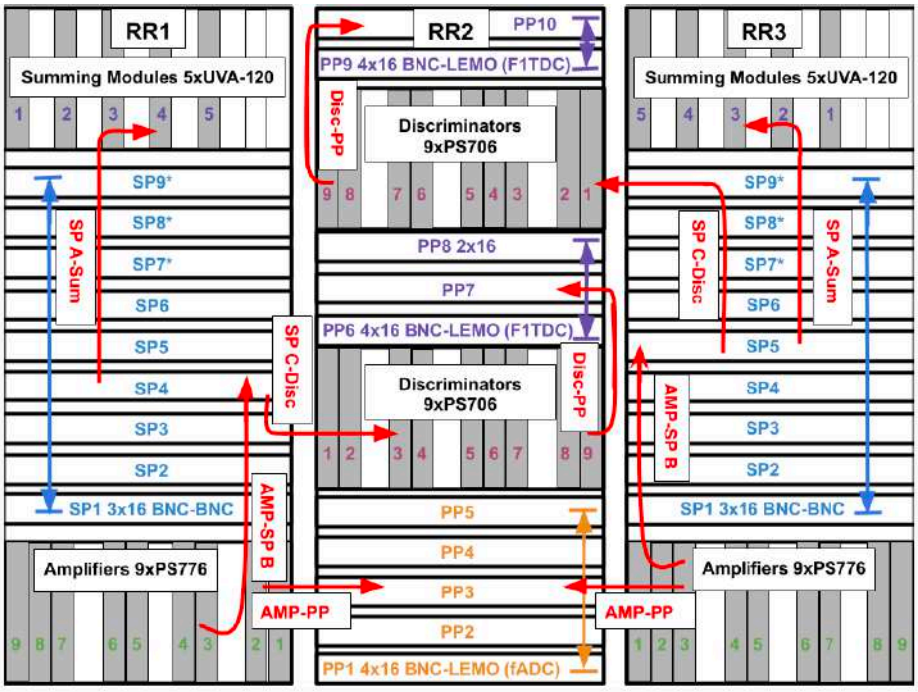

Figure 3.5: Front-end Electronics Layout for HCAL-J calorimeter.

the bottoms of racks RR1 and RR3; while, RR1 and RR3 are mirrored and each handle half of the 288 HCAL-J channels. These electronics are connected together via a series of cables, patch panels, and splitter panels.

So the path is as follows: beginning at the detector PMTs the physics signal can be traced to the fADC250s which make both energy and timing measurements; the analog signal exits the detector PMTs and enters the PS776 amplifiers at the base of RR1 and RR3 depending on from which half of the detector the signal originated. The PS776 amplifiers have dual outputs which each produce a 10 x amplified analog signal; from one of these outputs the amplified physics signal flows to patch panels in the bottom of RR2 which connect to DAQ side patch panels at the base of

RR4 via 100 meter long BNC cables. Once emerging from RR4 on the DAQ side the signals flow into the fADC250s in RR5 and are recorded for analysis.

For the timing measurement, the detector signals flow to the F1TDCs, as follows: an analog signal first exits the detector PMTs and flows into the amplifiers at the base of RR1 and RR3 (depending on from which half of the detector the signal originated); exiting the second of the two PS776 outputs the amplified analog signal travels to a 50-50 splitter panel with two sets of outputs. The halved signal then exits the first set of these outputs and travels to PS706 discriminators with low thresholds in RR2; this now NIM logic signal passes into BNC-BNC patch panels in RR2 and then over 100 meter long BNC-BNC cables which connect to BNC-BNC patch panels in RR4. After leaving the patch panels the physics signals enter a second set of discriminators which ensure the signal shape continues to have a sharp leading edge; the second set of discriminators translate the signal into an ECL signal which then flows into the F1TDCs over ribbon cables to be recorded.

3.2.2 DAQ Electronics

The electronics [33] composing the DAQ of HCAL-J is spread over two VXS crates, connected by an optical fiber, containing the individual ADC and TDC modules; the upper VXS crate contains five F1TDCs as well as two fADC250s, while the lower crate contains the remaining 16 fADC250s. Therefore, 18 fADC250s read the signals from the 288 HCAL-J modules

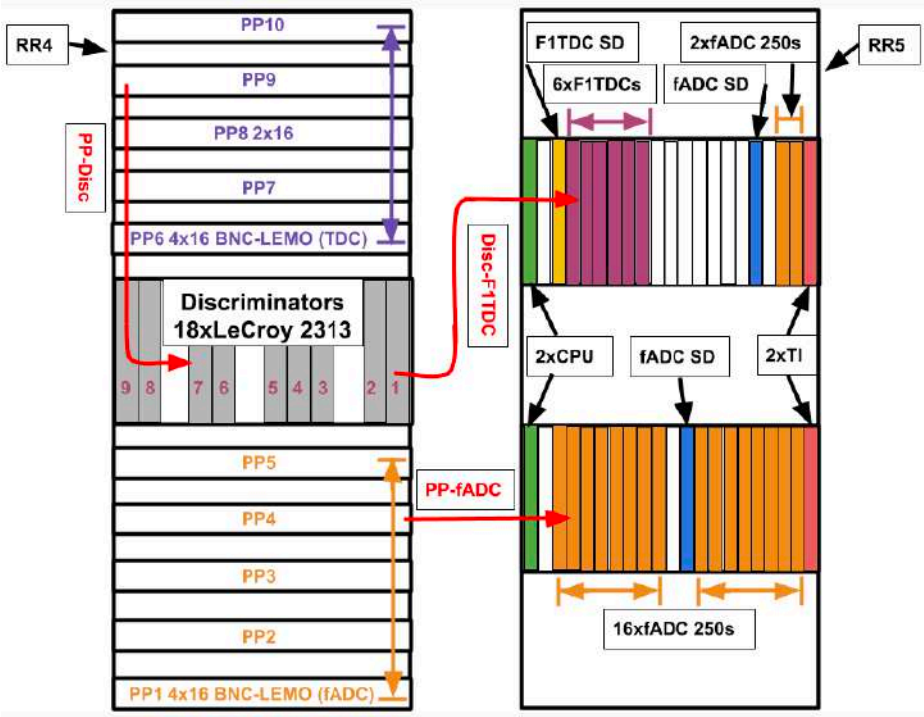

Figure 3.6: HCAL-J DAQ Layout.

via 16 LEMO connector inputs on each front panel, and collect it information about timing and energy.

Energy measurements are made by recording the voltage of the analog PMT signals which are proportional to the energy deposited in HCAL-J's scintillators.

Additional timing information for HCAL-J is measured by five F1TDC modules to record all 288 detector module signals. The F1TDCs feature both programmable timing windows and latencies for observing the signals from the detector modules.

3.3 Data acquisition system

HCAL-J integrates with the standard Jefferson Lab Hall A data acquisition system, [33]. A core part of this setup is the CEBAF On-line Data Acquisition System (CODA) created by the Jefferson Lab data acquisition group. CODA runs on VME and VXS crates containing the individual DAQ modules using the VxWorks operating system as well as on Linux workstations. CODA is controlled via the RunControl process which allows users to start and stop data runs, reconfigure the DAQ setup, and monitor the status of DAQ components via a GUI interface [34].

3.4 Geant4 Simulations Results

Carnegie Mellon University, in collaboration with JLab, developed G4SBS (a Geant4 based Monte Carlo application), [35], and did simulations about HCAL1, the first prototype from COMPASS, and HCAL-J, the definitive model, to evaluate the PMTs, the WLS and the performances of the complete modules.

For the simulations, the other BigBite detectors were not included, and only the calorimeter HCAL-J and the SBS magnet (a former 48D48 magnet that was previously used at Brookhaven National Laboratory) are included. The Fig.3.7 shows a single scattered event from the target. For visualization purposes, the front plates in HCAL were not displayed, but were present in the simulation.

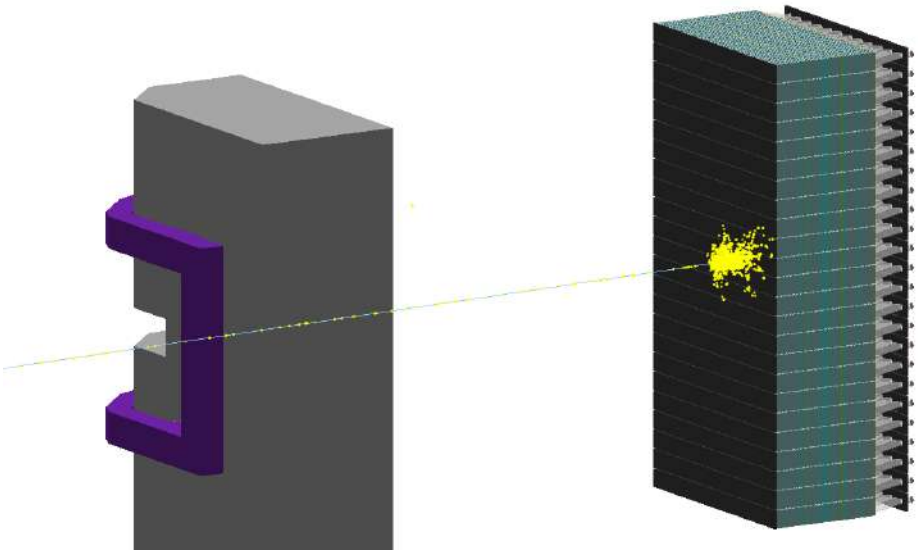

Figure 3.7: A single HCAL-J module as defined in the Geant4 simulation g4SBS. The full details are used only when optical photons are enabled, and in most cases a simplified model of the light-guide at the end is used, such as in the simulations used in this report.

3.4.1 Simulations Results

Simulations were performed for the seven Q^2 points planned for the GMn experiment, which correspond to scattered hadrons with momentum ranging from $\sim 2.5 GeV/c$ to$\sim 8 GeV/c$.

For each proton (neutron) the total energy deposited E_p (E_n) on all the scintillators in a 4x4 module cluster is recorded. Additionally, the (x,y,z) coordinate of the location in which the hadron first entered the boundary of the front plate is also recorded. Only events which reached the front plate of HCAL-J were considered.

Efficiency

The hadron detection efficiency is thus defined as the total number of hadrons with $E_h > E_{thr}$ divided by all the events which reached the front plate of HCAL-J, where E_{thr} is the threshold defined as $\frac{1}{4}$ the energy of the peak of the energy distribution. Figure 3.8 contains the efficiencies of both protons and neutrons for the seven GMn Q^2 points, and the numeric results are also tabulated in table 3.1. From that table one can see that the proton efficiency can reach almost as high as 99%, while the neutron efficiency remains close to 95%,. This discrepancy can be explained by the fact that protons (or any charged particle) can undergo minimum-ionizing radiation as it transverses through the scintillators, while neutrons cannot. For a particle that travels the full length of HCAL-J, it will cross a total of 40 cm of scintillators, and thus deposit a total of $\sim 90 MeV$ in the scintillators. So for hadrons with lower momentum, the minimum-ionizing radiation lies above the threshold, and ends up increasing the efficiency at that setting.

Position Resolution

The position resolution was determined from the width of the the distribution of differences between the reconstructed position and the recorded position where the hadron crossed the front plate boundary. For each hadron, the x-coordinate and y-coordinate were determined separately, and correspond to the energy weighted reconstructed position in a 4x4 cluster as shown in equation equation 3.1 and then used to reconstruct

	Efficiency		X-Resolution		Y-Resolution	
P_h	Neutron	Proton	Neutron	Proton	Neutron	Proton
(GeV/c)	(%)	(%)	cm	cm	cm	cm
2.6	95.5	98.8	6.5	6.1	7.0	7.1
3.2	95.5	98.8	5.9	5.6	6.4	6.6
3.7	95.3	98.3	5.4	5.2	5.6	5.7
5.2	94.6	96.4	4.5	4.5	5.1	5.2
6.3	93.9	95.6	3.8	3.8	4.5	4.5
7.3	93.7	95.1	3.4	3.4	3.9	4.0
8.1	93.3	94.7	3.2	3.2	3.8	3.8

Table 3.1: Simulations results for GM_n experiment.

the position of the incident hadron.

$$x = \frac{\sum x_m E_{h,m}}{\sum E_{h,m}} \tag{3.1}$$

Where x is the reconstructed coordinate, either x or y, then for a given module m, x_m is the central position of the module, either the x-coordinate or the y-coordinate, and $E_{h,m}$ is the energy deposited by a hadron in that module. The cluster was centered on the module with the highest energy, and included all modules from $[r-1, c-1]$ to $[r+2][c+2]$, where r and c are the row and column of the module with the highest energy. To ensure a full cluster would be made, no cluster was considered if the module was in the first and last row, or the first and last column. Figure 3.9 shows the expected position resolutions for all Q^2 kinematic points in GMn, and the numeric results are tabulated in table 3.1.

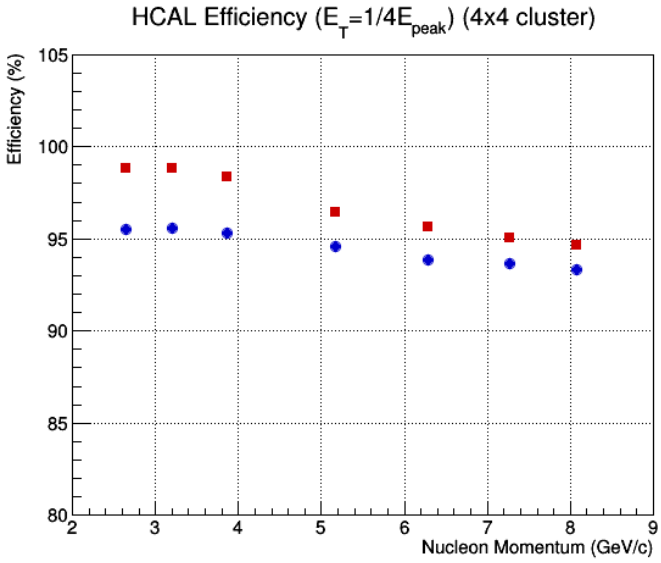

Figure 3.8: The detection efficiencies for both protons (red) and neutrons (blue) for all seven Q^2 kinematic points for GMn.

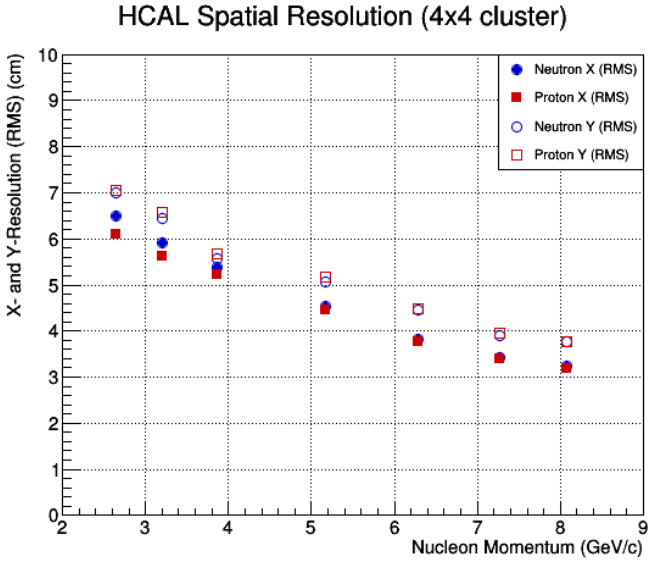

Figure 3.9: The position resolutions for both protons and neutrons for all seven Q^2 kinematic points for GMn.

Chapter 4

GEM Simulations

In order to study the detailed behavior of the GEM tracker, to be able to better fully understand the tracker response and therefore the performances, a series of simulations have been carried out; in the course of this chapter we will see the tools used to create the simulation models and the simulations themselves, and the results obtained in terms of gain and efficiency of the triple GEM detectors.

4.1 Software And Tools

For the microscopics simulations, the essential instrument is offered by the GARFIELD++ library; this one, implements with a certain degree of accuracy, all physical processes related to the production and multiplication of the charge inside a GEM module, as described in the next section. GARFIERLD++ need to be complemented by the structural model (3D geometry and materials) in the presence of electrostatic field of an ele-

mentary cell of a single GEM chamber (drift plane, GEM sheet and readout plane) and an analysis software of the charge distribution obtained on the readout plane, under different conditions.
To carry out these tasks, two different tools were used: ANSYS, for the 3D modeling of the elementary geometry and to obtain the map of potentials in every point of space, and ROOT for the analysis.

4.1.1 ANSYS Software

ANSYS [36] is engineering software, distributed by Ansoft, useful to create complex geometries, assign materials to the different generated volumes, and create electrostatic field solutions after assigning the boundary conditions of the electric potential and defined the nature of the materials.
There are a number of different packages that can be used in ANSYS including finite element analysis programs, structural analysis, of computational fluid dynamics and heat transfer; specifically for this thesis work, ANSYS MECHANICAL APDL was used, with ANSYS Parametric Design Language, where is possible to work by building "scripts" in the ANSYS programming language.
The construction of the ANSYS simulation model involves 3 different phases:

- Pre-processor step;
- Solution step;
- General Post-processor step.

Pre-processor

This is a fundamental part, that is the modeling; in this step you need to define the type of model you want to create, create the geometry with the respective materials and features, and choose the right mesh scheme to use.The first thing to do is choose the type of elements in which subdivide the starting domain; in fact, ANSYS allows you to choose among more than 150 elements in which each element is identified by the name of the category to which it belongs followed by a number.
In our case, the SOLID123 model was chosen which is a useful structure for constructing 3D solids with irregular meshes to which it is possible to apply potentials and generate electrostatic fields; moreover, the SOLID123 element is one of the few elements with which the GARFIELD++ library interfaces.
To build the actual geometry, ANSYS has many commands for creating three-dimensional solids.
In the specific case of the GEM tracker, we started choosing a primitive cell, Fig. 4.1, and a volume around it, so between the drift and readout planes; the primitive cell is the smallest unit of a volume that still possesses the characteristic properties of the volume itself and that if replicated in space several times, it allows us to obtain the entire volume.
The procedure followed to create a geometric model identical to that real one is the following:

- create the GEM primitive cell, consisting of rectangular parallelepipeds (box) for the two thin layers of copper with a thickness of 5 μm each, separated by a box of dielectric material with a thickness of 50 μm;

Figure 4.1: Primitive cell, realized with ANSYS.

- drill the primitive cell according to a biconical geometry with external diameter of 70 μm and internal diameter of 50μm; a complete hole is realized in the center of the cell, while the edges of the cell have a quarter hole each, Fig. 4.2;

- create a box that contains the above GEM foil centered at $z = 0$ and including the gap toward the drift plane at $z = 3$ mm (or the previous GEM foil at $z = 2$ mm) and the gap toward the readout plane at $z = -2$ mm (or the next GEM foil at $z = -2$ mm).

The above geometry can be triplicate to obtain the primitive cell of the triple GEM module.

At this point, it is possible to apply a meshing operation for our model,

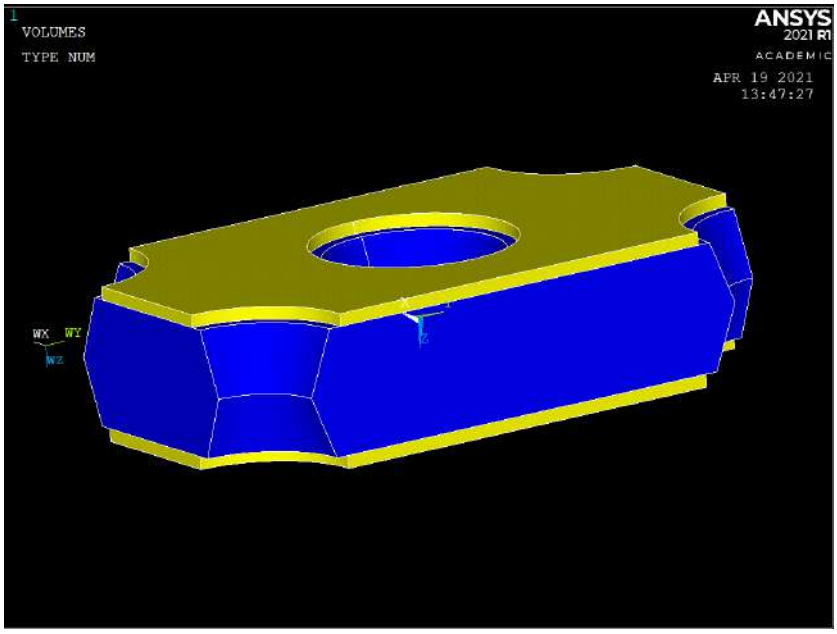

Figure 4.2: Primitive cell of a single GEM foil, with different material (yellow for copper and blue for Kapton) where we can look the biconical holes.

that means to define the subdivision into finite elements; during this operation, it is important to specify the material of each volume on which to create the mesh, and after this, ANSYS generates automatically the nodes and elements of our model.

In this phase it is possible to choose the type of algorithm used by ANSYS to generate the mesh, the size of the meshes themselves and the volumes on which we want apply what is specified; for our model the choice was a tetrahedral mesh, and with the "smart size" option it was assigned to the algorithm the possibility of choosing different mesh sizes, depending on the shape and size of the considered volume, Fig. 4.3, 4.4.

After completing the geometric part, and after defining the appropriate

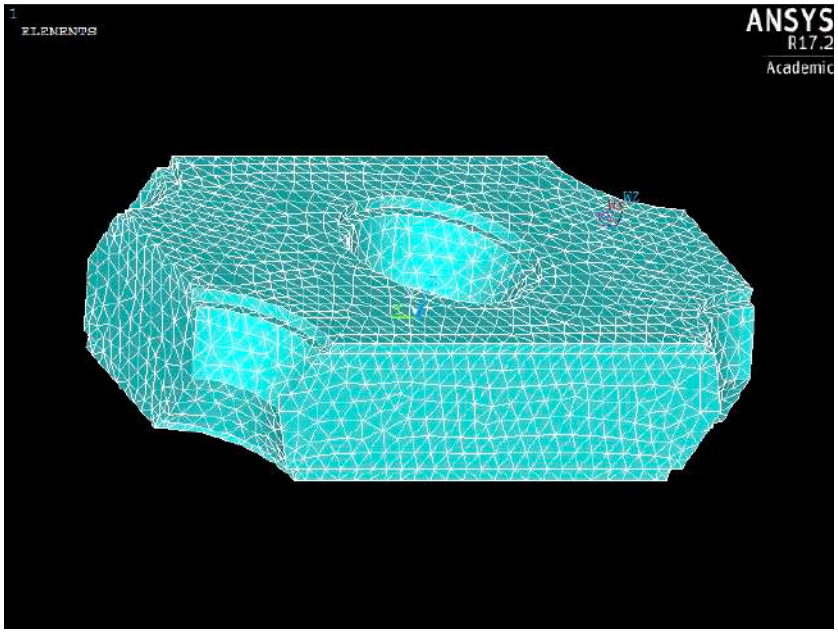

Figure 4.3: Primitive cell of a single GEM foil, after meshing operation.

characteristics of the materials (dielectric constant, resistivity, etc.), it is necessary to define the boundary conditions of the electric potential, assigning the appropriate voltages to the different volumes; therefore, we must apply the appropriate potential differences to the metal elements of the model (readout plane, lower and upper plane of the GEM primitive cell, drift plane). So, we have to set the readout plane at 0 V and apply negative and decreasing potential values, up to the drift plane.

Solution

After building the complete model with materials, meshes and tensions, it is possible to generate the electric field solutions; it is important to specify that, if we have a dense mesh, we also have a very high number

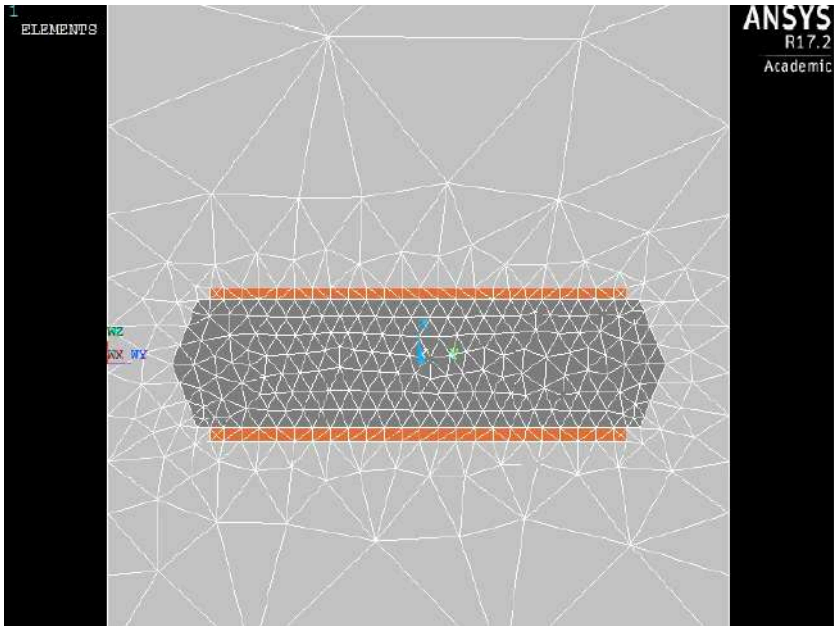

Figure 4.4: Detail showing the meshes made on the gas in light gray, on the copper in orange and on Kapton in dark gray. It is possible to see how in the primitive cell the meshes are more dense than in the gas part ant this is a consequent of the option "smart size".

of nodes and consequently a numerical solution that closely approximates the analytic solution. On the other hand, a too dense mesh is superfluous in the regions of weakly variable field and can significantly burden the modeling and consequently also the simulation process.

At this point, it is possible to launch the model solution using the Solve option and specifying the type of solution, in our case Current LS; in this regard, it is useful to say that ANSYS solves the Poisson equation through numerical finite element calculus, using as boundary conditions the values of the potential that we assigned to the different metal planes.

General Post-processor

In this phase it is possible to check the results of the analysis and their quality, and check the parameters that denote the accuracy of the presented solution.
Shows as an example, the potential map obtained in one of our model. After completing the modeling phase, the solution phase, and results visualization phase, it is possible to save the files which will be inserted as input in the C ++ code developed for GARFIELD++; in particular the files that we need to implement the simulations are:

- MLIST.lis: contains the characteristics of the used materials;
- NLIST.lis: provides the list of model geometry nodes, with the respective coordinates;
- ELIST.lis: contains nodes and elements of the model, considering the meshing operation;
- PRNSOL.lis: provides the potential at each node of the model.

4.1.2 Open Source GMSH and ELMER

The geometrical and electrostatic model of the primitive GEM cell has also been obtained using the open source GMSH [https://gmsh.info/] and ELMER [https://www.csc.fi/web/elmer] software.
GMSH is a 3D finite element mesh generator; the geometry can be defined using the GMSH own scripting language (as for ANSYS); once the

geometry is defined, GMSH may produce the output mesh choosing between different predefined algorithms; the visual quality of the GMSH generated meshes are generally lower than for ANSYS ones.
ELMER is the multiphysical simulation software that includes the numerical solver of electromagnetic models, analogously to the "Solve" option in the integrated ANSYS modeler. ELMER can ingest the GMSH output meshes, it accepts the potential boundary conditions similar to ANSYS and can solve the corresponding Poisson Equation (StatElecSolve directive in the ELMER scripting).

4.2 GARFIELD++ tool

GARFIELD++ [37] is a toolkit used for detailed simulation of gaseous detectors.
It is a software developed at CERN and derived from the original GARFIELD++ library, that uses the C++ programming language and owns a user interface generated by ROOT (data Analysis Framework)[38]; for this very reason it can access all existing ROOT libraries.
GARFIELD++ uses HEED libraries, simulate the ionization and the transport of charged particles (electrons and ions) in a mixtures of gas (in the presence of electric and magnetic fields).
In addition to allowing the generation of electromagnetic fields under simple geometries conditions, GARFIELD++ is able to use fields maps, in two and three dimension, calculated with finite element programs as:

- ANSYS;

- Elmer;
- Comsol;
- CTS.

GARFIELD++ essentially looks like a library that requires the definition and implementation, in C++ language, of the relative simulation code, which must essentially manage the inputs, the generation flow of the events and the outputs.
Initially, the implemented code loads the .lis files (generate using ANSYS in our work), containing all the information about the primitive GEM model; it is possible to use replication functions along the X and Y axes (in our case with spatial periodicity respectively of 140 microns and 242 microns), in order to exploit the symmetry of the GEM foil in these directions, to create chambers with dimensions greater than the primitive cell. GARFIELD++ interfaces with the Magboltz library to define atomic characteristics and thermodynamic conditions of gas mixtures under operational conditions; through this function it is possible to enter the type of gas, its temperature and pressure. In our model, a mixture of 70% Argon and 30% of CO_2 was used, the temperature of the mixture is 293.15 K and a the pressure is 760 Torr.
Numerous parameters can be set from the command line including:

- the type of the primary particle, for example protons or electrons;
- the energy of the primary particles;
- the number of the primary particles;

- the simulations volume;
- the incidence direction (angle) of the primary particle;
- the impact point of the primary particle.

For each primary particle, the code follows its path up to the readout plane and generates the ionizations according to the theoretical models implemented in HEED. The produced particles are transported along the field lines and trigger the avalanches production as they pass in the region of the holes.
Part of the electrons and ions are stopped on the metal sheets that delimit the GEM foil; some electrons can also be stopped along the holes walls. Both effects are considered in the simulation code, for the purposes of quantitative assessment of system efficiency losses.
Using the ROOT libraries, it is possible to view and save the results of the simulated event: for example the "physical" event of creation of the avalanche, in Fig. 4.5, the electric field mapping inside the hole, in Fig. 4.6, the distribution of the avalanche on the readout plane etc.

4.3 Microscopic Simulations

In order to investigate the performance of the triple GEM chambers, developed for high luminosity experiments with the Super BigBite Spectrometer at Jefferson Laboratory, we made a flexible and efficient multistep simulation processor based on ANSYS for the geometry and the electrostatic field and then combined to GARFIELD++.

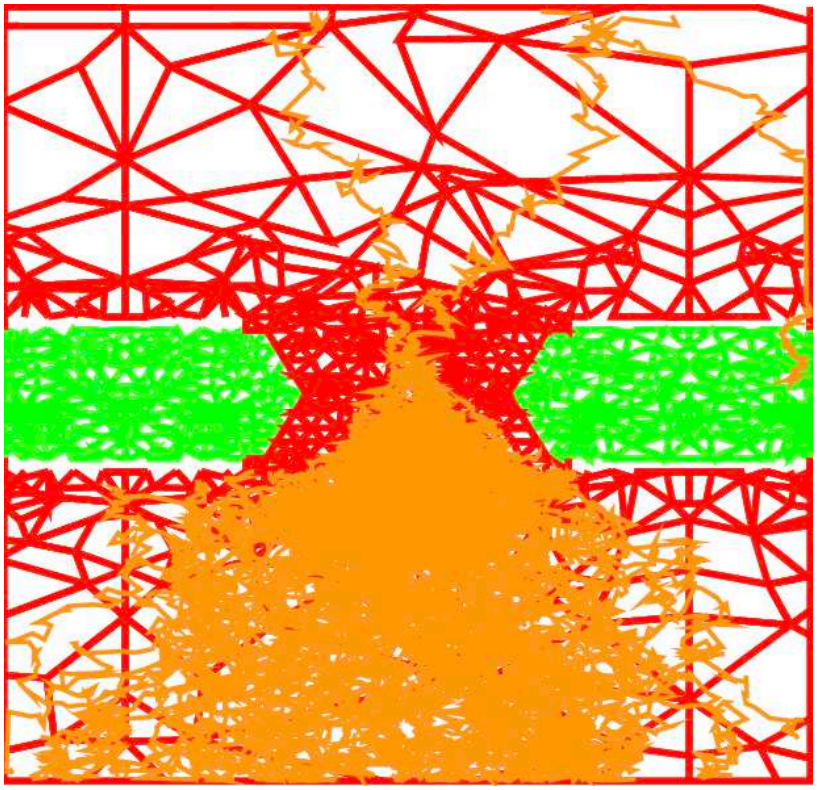

Figure 4.5: Plot of the avalanche inside a GEM hole; green: the kapton mesh, red the gas volume mesh, orange the charged primary and secondary electrons.

It is important to underline that some simulations reported in this chapter used a CAD model created with GMSH + ELMER instead of ANSYS.

4.3.1 Simulations Models

For this thesis work we built two different models to carry out our simulations: a Multistep Model and a Full 3GEM Model.

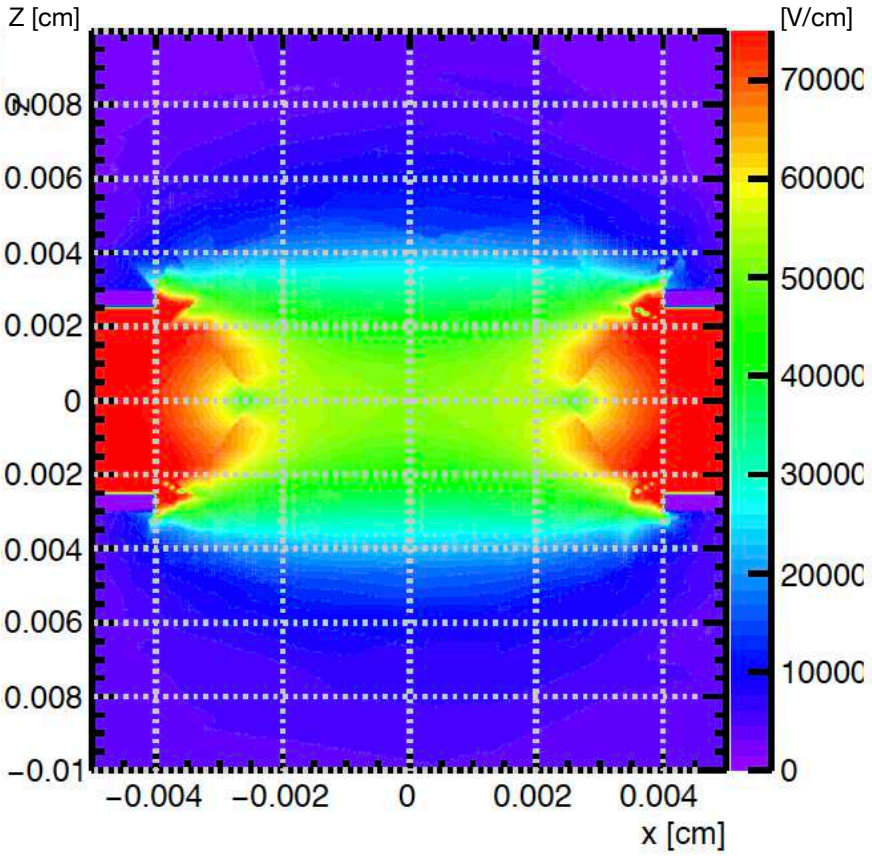

Figure 4.6: Electric Field map inside a GEM hole.

Multistep Model

The Multistep Model is composed of 3 GEM foils and the readout plane; the particularity of this model is that each components is independent from the others. This approach is useful to analyze different schemes, imperfections and foil misalignment using the same microscopic simulations. As schematically represented in Fig. 4.7, the single block model includes a central foil and the border of the previous and following foils

while the sensitive volume where the particles are simulated, is limited by the mid-planes of the gaps between foils. Each block is simulated separately: the outcome (electrons end-points) of the previous block is fed into the next block, which can be rotated and shifted with respect to the previous one by an appropriate coordinate transformation [39].

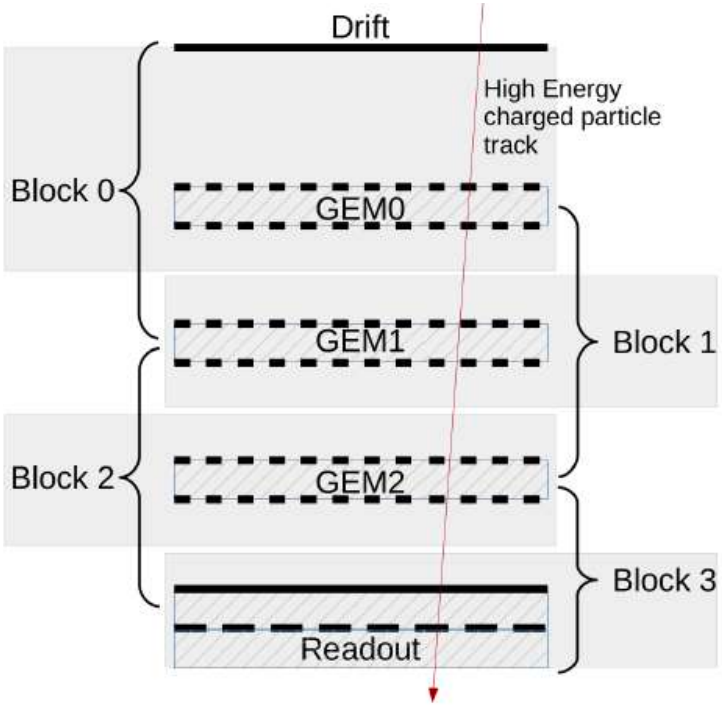

Figure 4.7: Schematic view (not to scale) with the definition of the different blocks of simulation (curly brackets) used in the multistep approach.

Full 3GEM Model

The full 3GEM Model is instead, Fig. 4.8, a complete configuration where the primary particle start from the drift plane, crosses the first, the second

and the third GEM foil and stop it in the readout plane. In this model, it is possible to evaluate the simulations results only in the readout plane. The different GEMs are "perfectly" aligned in order to optimize the single cell mesh size.

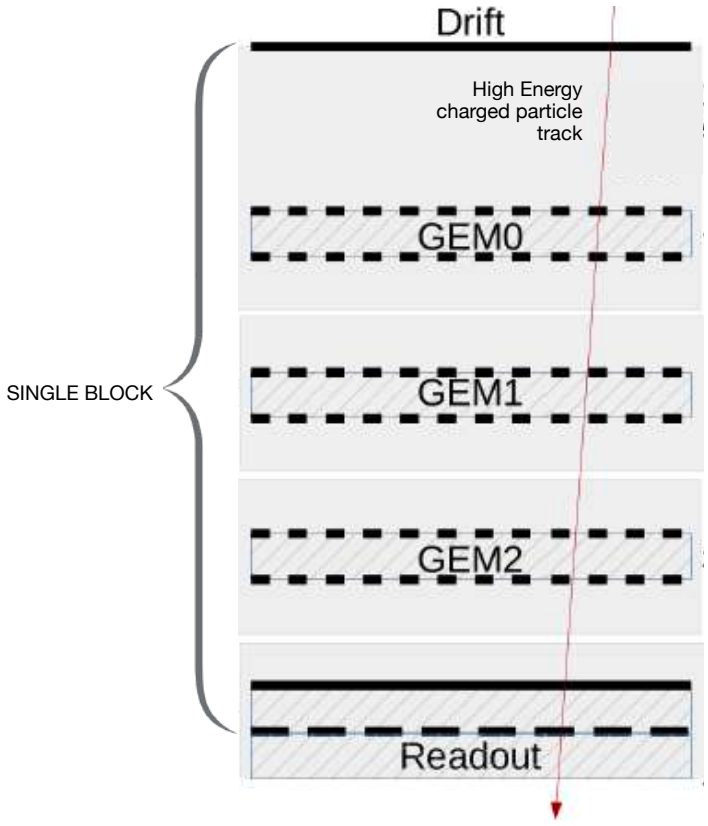

Figure 4.8: Schematic view (not to scale) of the full 3GEM approach.

4.3.2 Simulations Results

For the preliminary simulations, useful to validate the model and the relative results, we used the Multistep approach and, using electrons with

energy of 4GeV as primary particles, we were able to evaluate: the distribution of the charge in the readout plane, the quantity of charge in this last, the time and the energy of the particles in the readout plane.
Below, Fig.4.9,4.10, reports typical distributions obtained from the simulations: x and y spatial distributions (which shall be very similar), arrival time distribution and energies of the avalanche electrons.
50 primary electrons with energy of 4 GeV were simulated, in the condition of the incident particles perpendicular to the readout plane, and that pass through the center of the hole.

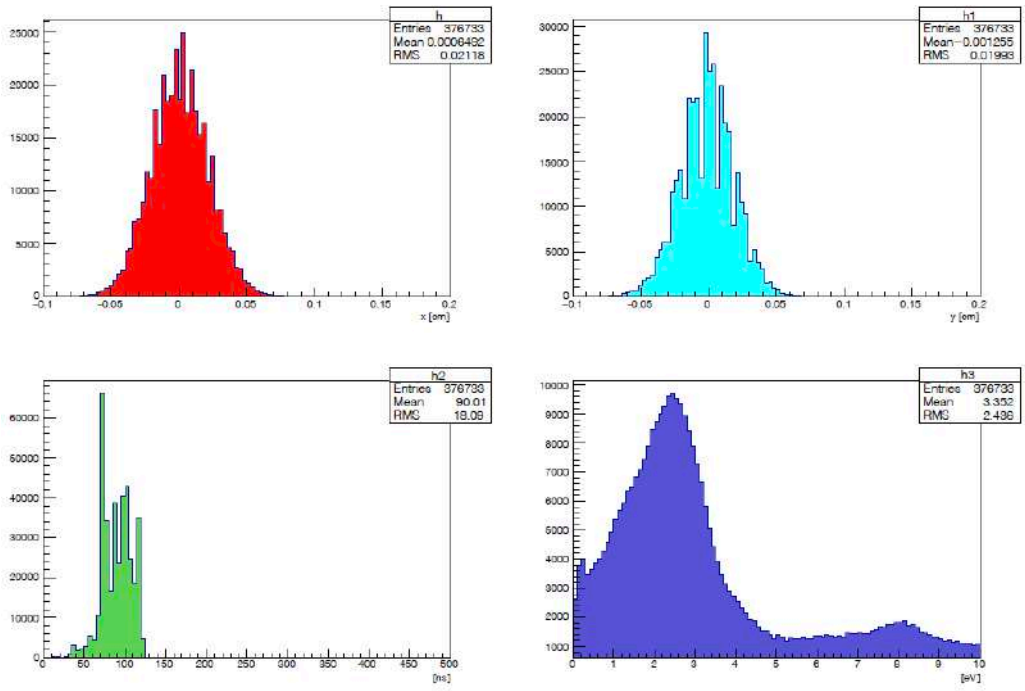

Figure 4.9: Top left the distribution in x-axis of the collected charge, top right instead the distribution in y-axis. Below left, the distribution of arrival times, while in the lower right, the energy distribution of electrons in the readout plane.

These distributions are reasonably consistent based on simplifying considerations based on diffusion values (diffusion coefficient in argon about $D = 200 - 300\frac{cm^2}{s}$) and typical drift velocity of the secondary electrons (around $5 - 6\frac{cm}{\mu s}$). In fact, assuming a distance of about 0.9 cm, the maximum crossing times of the entire GEM is about 150 ns, while the distribution of the avalanche is $\sqrt{2 * D * t} \sim 90\mu m$ (without the multiplication of GEMs).

An example of the detailed evolution of the electron avalanche is presented in Fig. 4.10

Furthermore, the characteristics of the charge collection were investigated when the angle of incidence of the particles varies and when the primary particles changes directions from the point of impact on the x-axis with respect to the center of one of the holes.

Charge Distribution on the readout plane

The charge distributions on the readout plane was evaluated, when the impact point of the primary particles varies respect to the center of the hole; in particular the simulations were performed with 10 electrons, with incidence perpendicular to the readout plane and varying the x coordinate. What emerges, Table 4.1, is that the distribution on the readout plane and the avalanche width do not depend on relevant way from the point where the primaries enter the GEM chamber.

This dependence has been confirmed with 61 simulations, each one with 10 primaries, in which the point of impact was randomly varied in a $70x70\mu m$, Fig. 4.11.

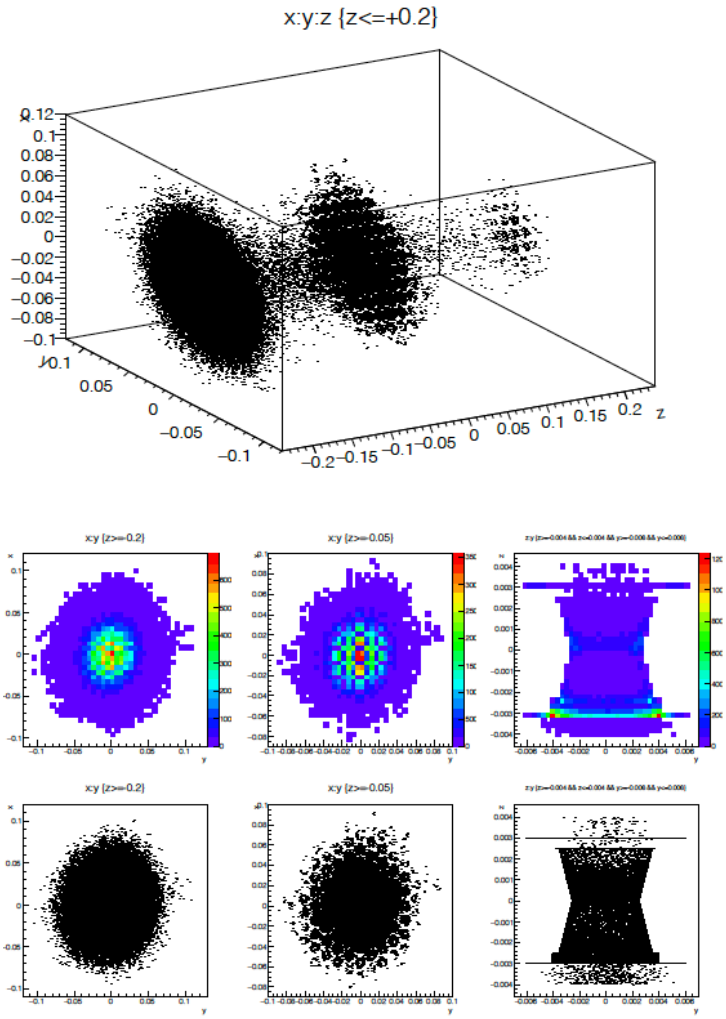

Figure 4.10: Map of the charge distribution on the readout plane on the left, on the last GEM sheet in the center and inside the hole on the right.

We did the same study but changing the angle of incident respect to the perpendicular to the readout plane; the results are in the following Table 4.2:

As expected, in opposition to the previous case in which the avalanche

X Coordinate	Angle	X distribution	Y distribution
x=0.0000 cm	0°	233 μm	213 μm
x=0.0035 cm	0°	214 μm	210 μm
x=0.0070 cm	0°	215 μm	206 μm

Table 4.1: Avalanche width on the x and y axis, at different x values.

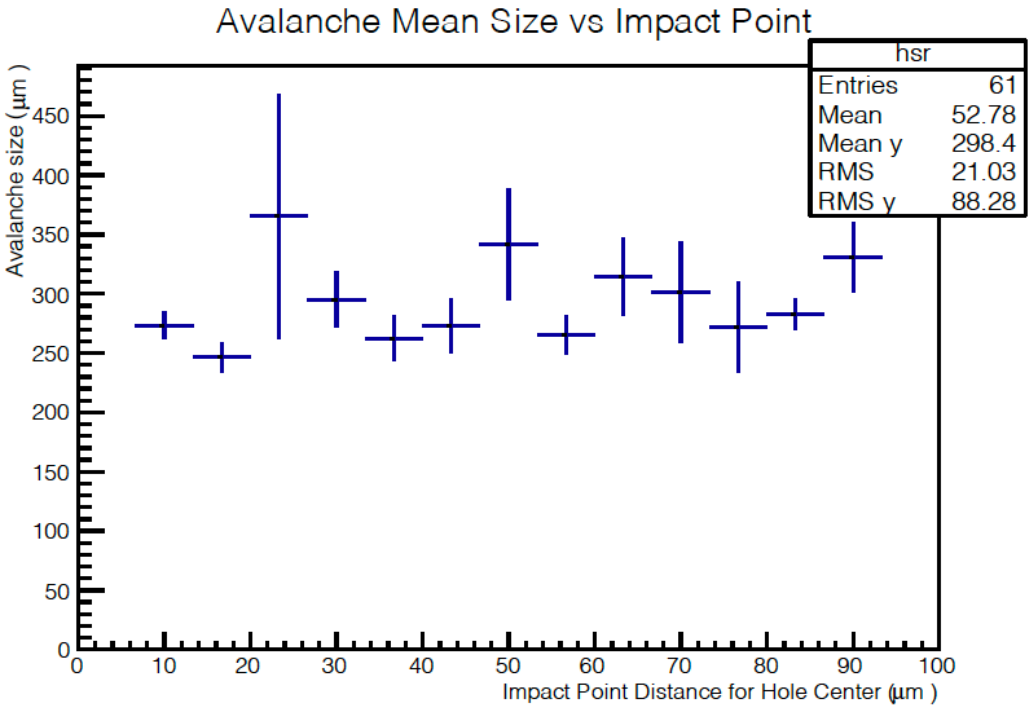

Figure 4.11: Avalanche Mean size versus impact point.

width does not depend from the impact point of the particle, we obtain a non negligible systematic changes in the avalanche size if the angle of incidence of the primary varies, Fig 4.12.

X Coordinate	Angle	X distribution	Y distribution
x=0 cm	0°	233 μm	213 μm
x=0 cm	10°	295 μm	298 μm
x=0 cm	30°	381 μm	398 μm

Table 4.2: Avalanche width on the x and y axis, at different x values.

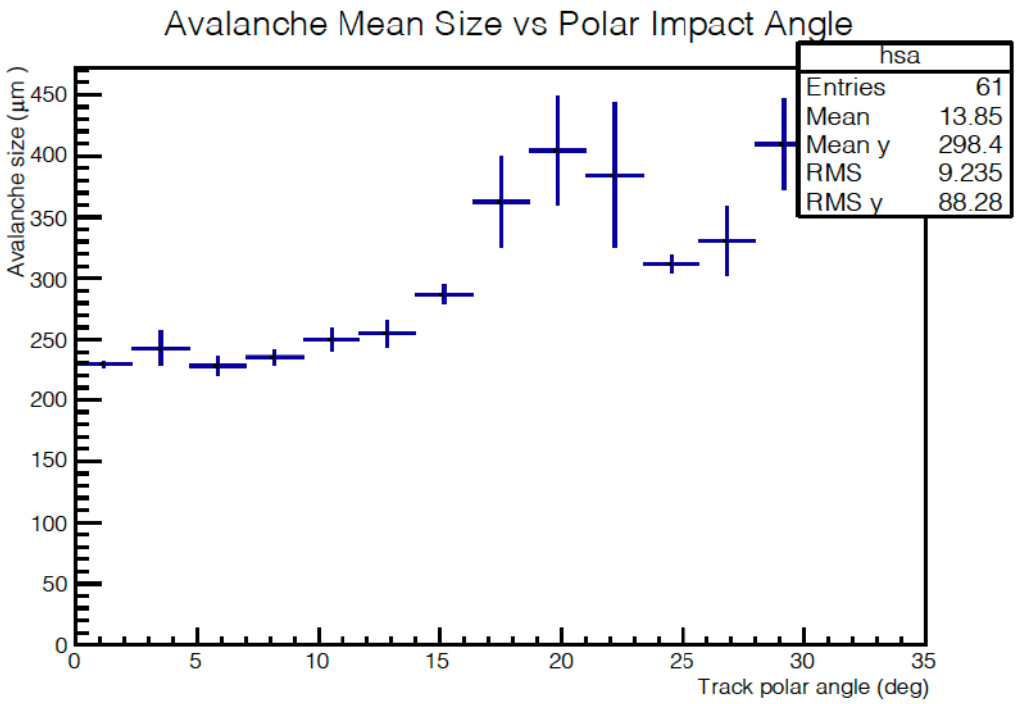

Figure 4.12: Avalanche Mean size versus polar impact point.

Gain

With a Triple GEM detectors, it is possible to reach a good gain using relatively low HV values; we define the module gain, the number of electrons collected on the readout plane for single primary particle.

We studied the gain obtained with two different series of simulations: 61 simulations with electrons of 4 GeV, Fig. 4.13, and 121 simulations with protons of 2.8 GeV, Fig.4.14; the impact point of the primary particles is random in a range between 0 and 0.007 cm in x and y, while the polar angle is random in a range between 0 and 30 degree.
These energy values are similar to those expected during the JLAB experiments and this angular range reflects the expected experimental conditions.

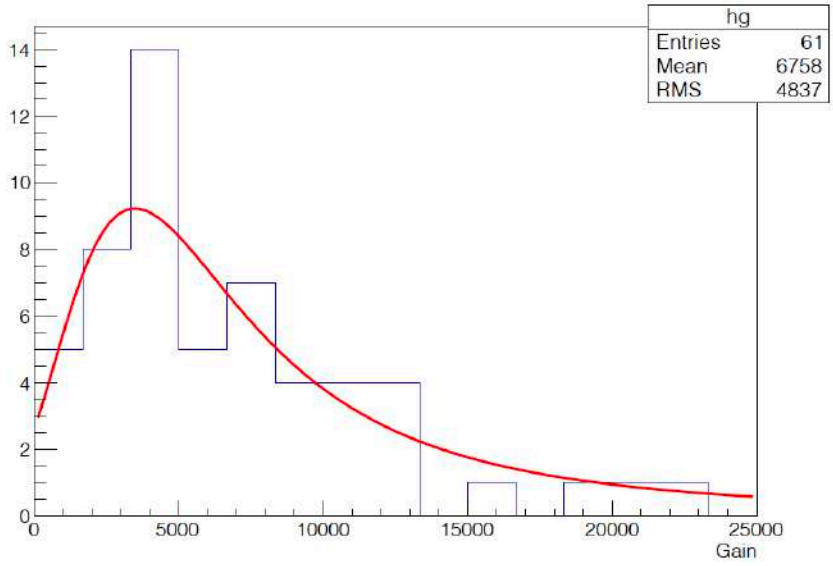

Figure 4.13: Landau fit of the distributions of the average gain of electrons arriving on readout plane.

It is useful to observe that the electrons and protons, when they cross a material, they lose an amount of energy of the same order of size but different in the two cases. The gain of the electrons is greater compared to that of protons when they pass through a material but in any case the

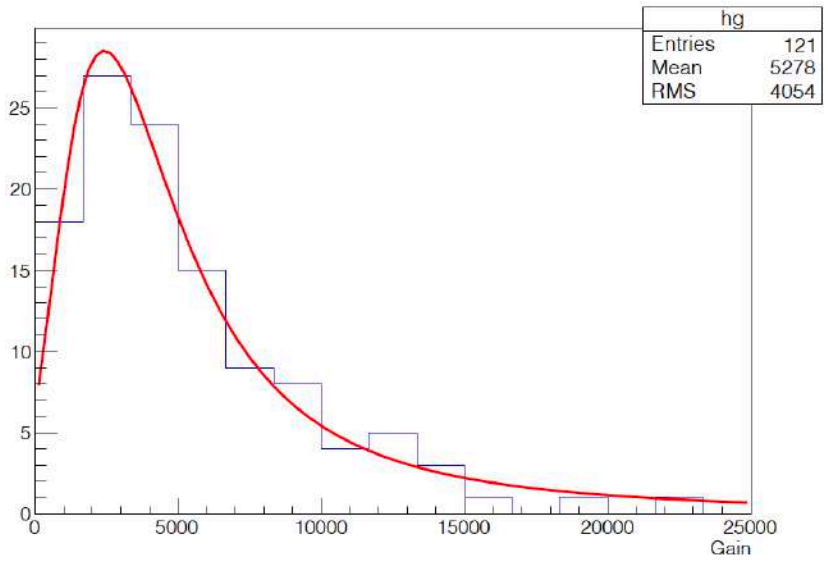

Figure 4.14: Landau fit of the distributions of the gain due to protons as primary particles.

obtained gain is corresponds with what was expected.
The collision $\frac{dE}{dx}$ given by the NIST ESTAR and PSTAR programs for Argon is assumed:

- 4 GeV electrons have $\frac{dE}{dx} = 2.497 MeV * cm2/g$
- 2.8 GeV protons have $\frac{dE}{dx} = 1.530 MeV * cm2/g$

The ratio is about 1.63 and should correspond to the earnings ratio which instead is about 1.28. The relative difference is about 25% which can be considered as a rough estimate acceptable.

4.3.3 Comparison Between Simulations Results and Real Data

A proton beam with energy of 2.8 GeV, is available at the Juelich Research Center, in Germany, thanks to the COZY accelerator [40]; this beam was used to test 4 triple GEM modules with area of $40x50cm^2$ assembled for JLab.

The response of these modules was compared with a triple GEM reference module (Mod.0).

Different voltage divider resistors configurations were used to provide the High Voltage levels to each GEM module, as presented in Tab. 4.3, and therefore to obtain different GEM gains.

	R1 [Ω]	R2 [Ω]	R3 [Ω]	R4 [Ω]	R5 [Ω]	R6 [Ω]	R7 [Ω]	R8 [Ω]
Module 0	441 K	7.2 M	3.76 M	7.2 M	3.63 M	7.2 M	2.98 M	7.2 M
Module 1	441 K	7.2 M	3.92 M	7.2 M	3.57 M	7.2 M	3.57 M	7.2 M
Module 2	441 K	7.2 M	3.92 M	7.2 M	3.92 M	7.2 M	3.92 M	7.2 M
Module 3	441 K	7.2 M	3.76 M	7.2 M	3.63 M	7.2 M	2.98 M	7.2 M

Table 4.3: Voltage dividers values of Juelich modules.

The of the different dividers is the following: R1 is the resistor in series with the Power Supply, R2 connect the drift with the upper first GEM layer, R3 connect the two sides of the first GEM foil, R4 connect the bottom GEM layer to the upper of the next GEM foil, and so on till R8 which connect the last GEM bottom foil to the ground (readout).

All simulations have been performed for high energy protons at 2.8 GeV traversing the GEM with a uniformly distributed incident angle between 0 and 30 degree.

These data were used to start a comparison with the simulations data in order to calibrate and validate the simulator models.

The real gain results are in the following figure, Fig. 4.15, [41].

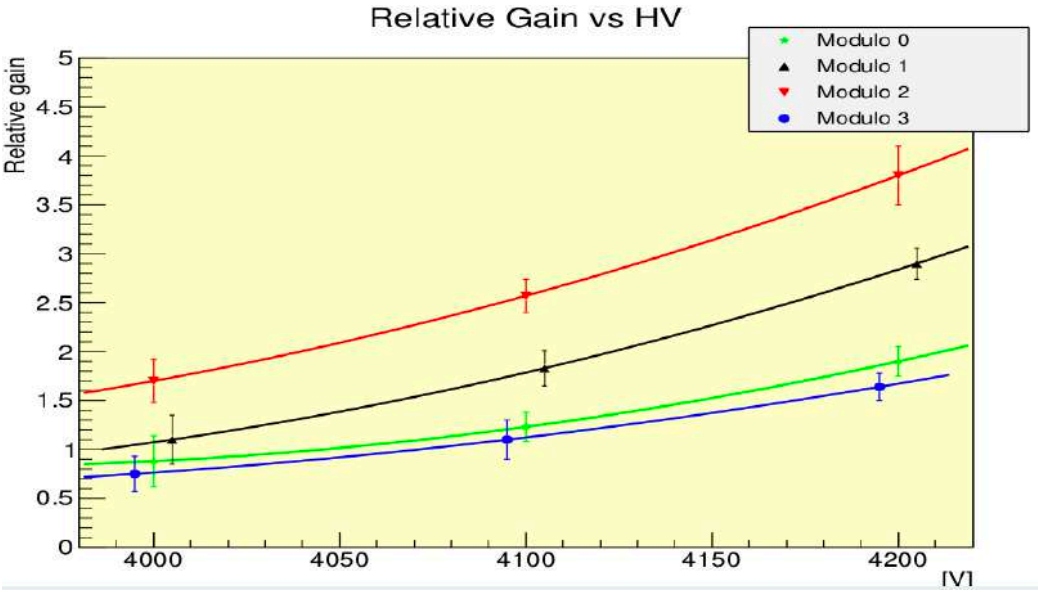

Figure 4.15: Polinomial Fit of the GEMs relative gain at different voltage, respect to the voltage reference chamber.

The Full 3GEM simulation model as been used for the comparison to the real data, since this approach permit to include the effect of the ion drifting toward the drift plane, and is expected to be more realistic; a comparison of the Full 3GEM and Multistep Model is underway but not yet consolidated due to the long processing time required by a single Garfield++

simulation in the available computational platforms (Intel-Xeon E5/16 cores with 32 Gbyte and Intel-i7-4770/8 cores with 16 Gbyte): a single primary charged particle simulation at nominal gain of about 8000 typically requires between 0.5 and 1 h of real time.
For all the modules about 1000 simulations were carried out with a primary proton of energy equal to 2.8 GeV; it is possible to observe, see next paragraphs, that this statistic is sufficient since all the quantities saturate after about 600 tracks.
The quantities, object of our study, relating to all modules at 4000,4100 and 4200 Volts, will be shown below; in particular, the drift time, the efficiency, the number of electrons generated by the first ionization of the incident particle, the total gain due to these secondary electrons and the charge distribution on the readout plane, in x and y axes, will be exposed.

Simulations parameters at 4000 V

Considering about 1000 simulations tracks we obtains, for all modules at 4000 Volts, the Total Gain in Fig. 4.16. The results about the studied parameter, for all modules at 4000 Volts are in the Fig. 4.17.

Simulations parameters at 4100 V;

Considering about 1000 simulations tracks we obtains, for all modules at 4100 Volts, the Total Gain in Fig. 4.18.
The results for all modules at 4100 Volts are in the Fig. 4.19

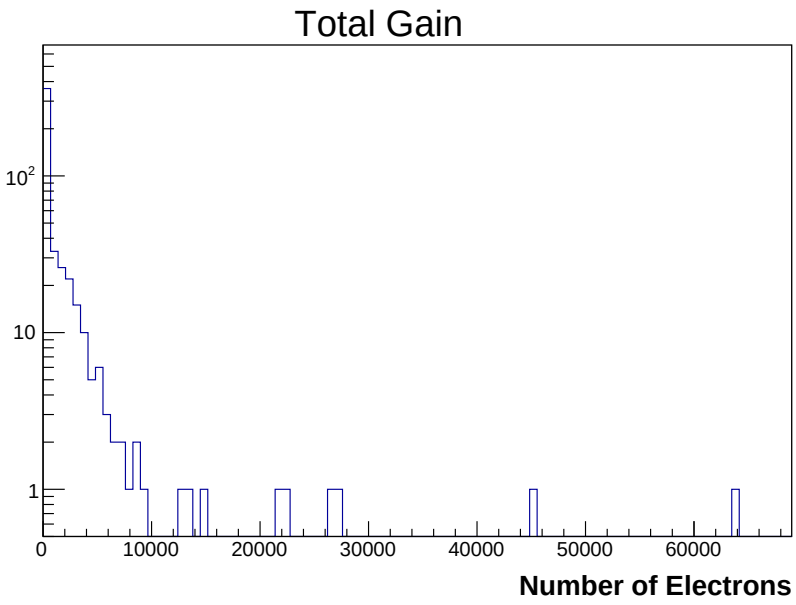

Figure 4.16: Total Gain for all modules at 4000 Volts.

Simulations parameters at 4200 V

Considering about 1000 simulations tracks we obtains, for all modules at 4200 Volts, the Total Gain in Fig. 4.20.
The results for all modules at 4200 Volts are in the Fig. 4.21.

Relative Gain from simulations

In conclusion it is possible to see in Fig. 4.22, the plot that relates the relative gain and the HV; remember that the relative gain is given by the ratio between the gain of the module and the reference one (Mod.0 at 4200 Volt).
Comparing the simulations curves and the beam-test curves we can observe that the relative gain, is generally underestimated by simulations;

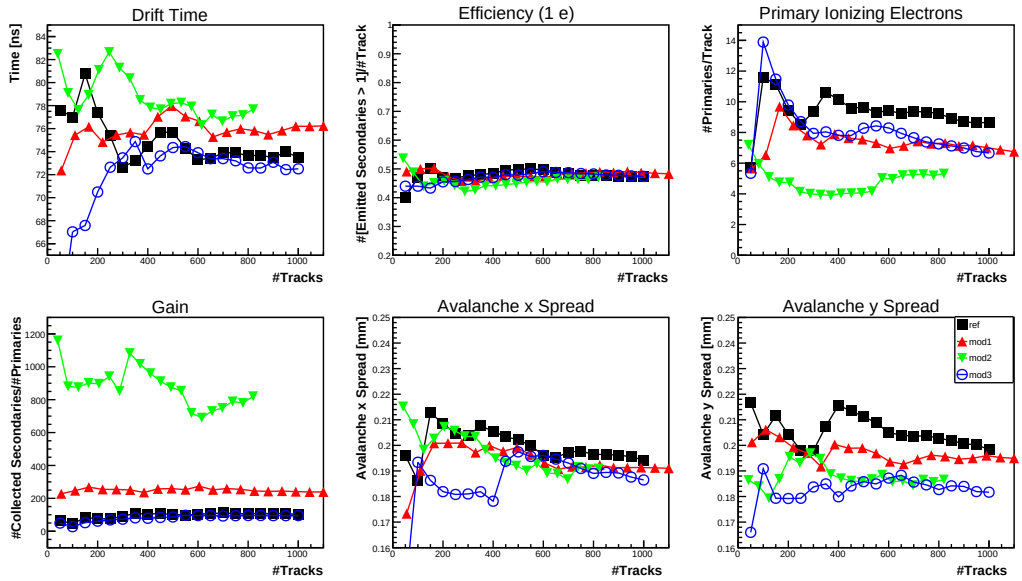

Figure 4.17: Parameters designed for all 4000 Volt modules; the parameters are averaged over the number of tracks cumulated in the corresponding x axes. The parameters tend to constant (stable) values above about 600 cumulated events.

the discrepancy is below 25 % for all modules except module 1 where it is about 50 % for all points (a systematic shift of the relative gain curve). Since it occur to the intermediate-gain module, this abnormal behavior can be more likely explained by a malfunctioning (or not correctly characterized) module or divider than by systematic deviation of the simulator unfortunately this hypothesis cannot be clearly confirmed since the tested module 1 is no longer available due to multiple shorts of its GEM sector during the integration tests. Further studies and comparisons are ongoing to validate the simulator against the upcoming commissioning data, and compare between the different implementations ANSYS vs GMSH-ELMER and Multistep vs Full 3GEM; unfortunately, as mentioned above

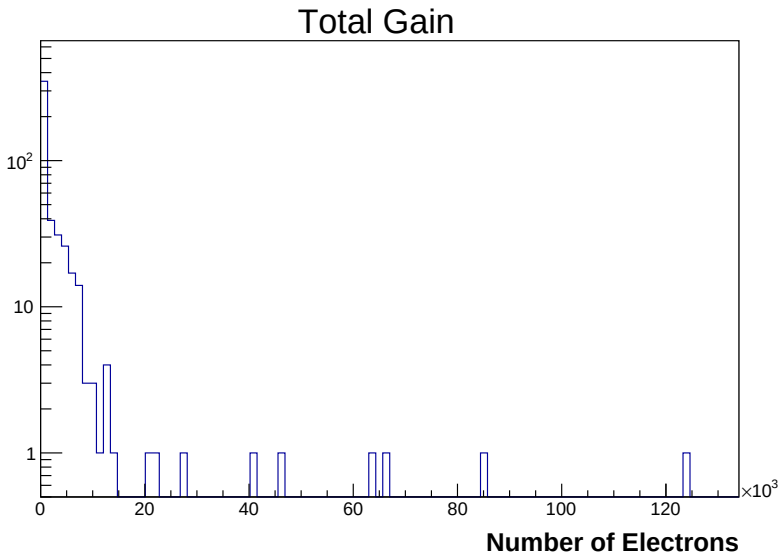

Figure 4.18: Total Gain for all modules at 4100 Volts.

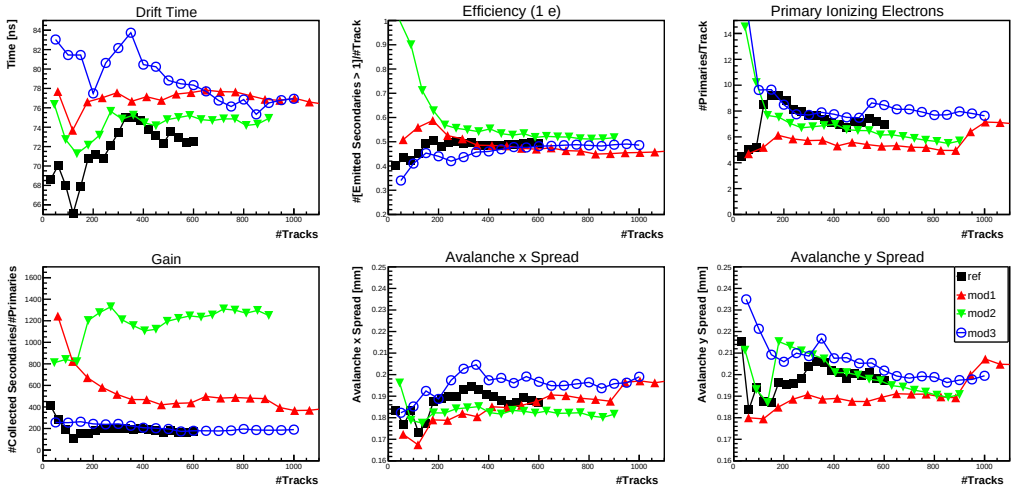

Figure 4.19: Parameters designed for all 4100 Volt modules; the parameters are averaged over the number of tracks cumulated in the corresponding x axes. The parameters tend to constant (stable) values above about 600 cumulated events.

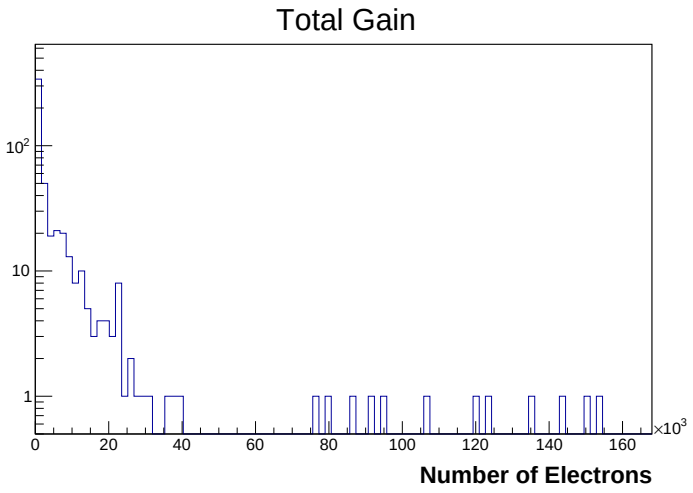

Figure 4.20: Total Gain for all modules at 4200 Volts.

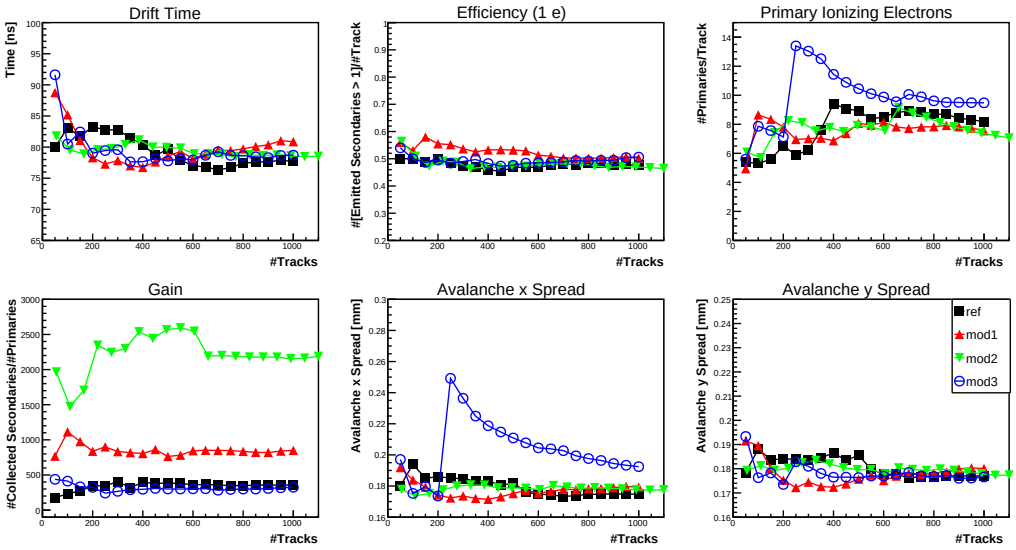

Figure 4.21: Parameters designed for all 4200 Volt modules; the parameters are averaged over the number of tracks cumulated in the corresponding x axes. The parameters tend to constant (stable) values above about 600 cumulated events.

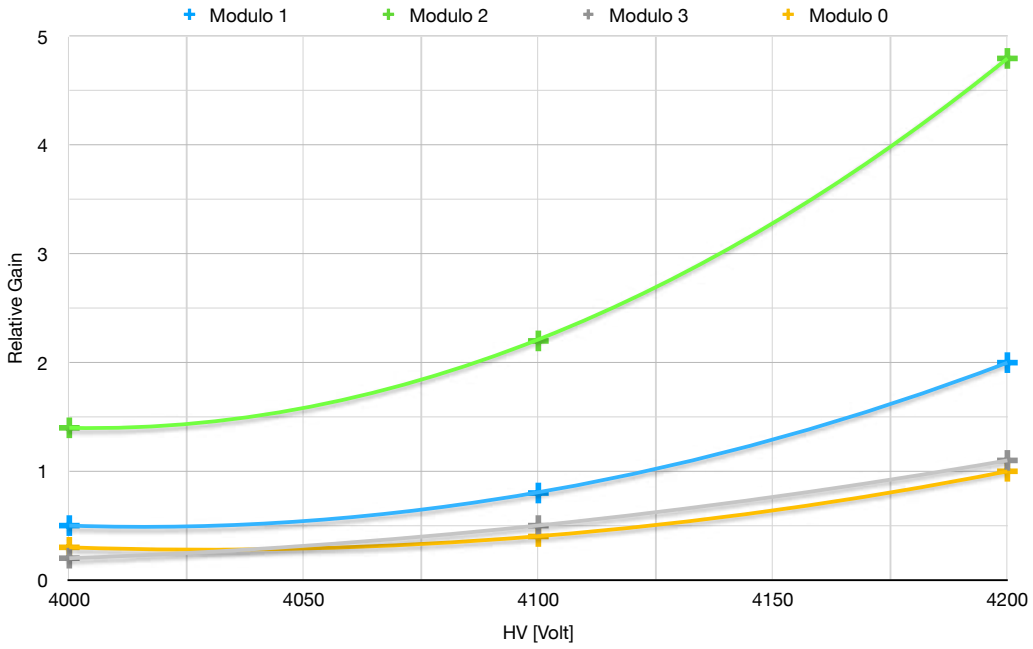

Figure 4.22: Polinomial Fot of the Relative gain VS HV, from simulations results.

the full Garfield++ simulation is extremely demanding in terms of computational resources; in this respect recent progress has been reported in literature [42] and the latest Garfield++ library version should include the optimized search of the proper electric field mesh during the avalanche simulation.

Chapter 5

HCAL-J Tests And Data Analysis

If for the Triple GEM the work was focused on simulations, for HCAL-J, the work was of calibration, cabling and testing, using cosmic rays or LEDs present in the calorimeter modules.

5.1 HCAL-J Test With 4x4 Matrix

During the summer 2018 the INFN Catania Group, in collaboration with HCAL-J JLab group, started the test of some HCAL-J modules using cosmic rays. The purpose of our test was the assessment of the performances of HCAL-J and its single components, before starting to use it for the experiments in Hall A at JLab.
We studied a 4×4 matrix of modules and respective PMTs, configured as shown in Fig.5.1; so we tested 16 HCAL-J complete modules using four trigger paddle placed on the top of the first subassembly. Totally, we used 24 signal long cables and 24 HV short cables (8 for the 4 paddles on the

top of the frame and 16 for the 16 modules of HCAL-J, [30]. It is possible to look each PMT and its signal using the event display macro, Fig.5.2

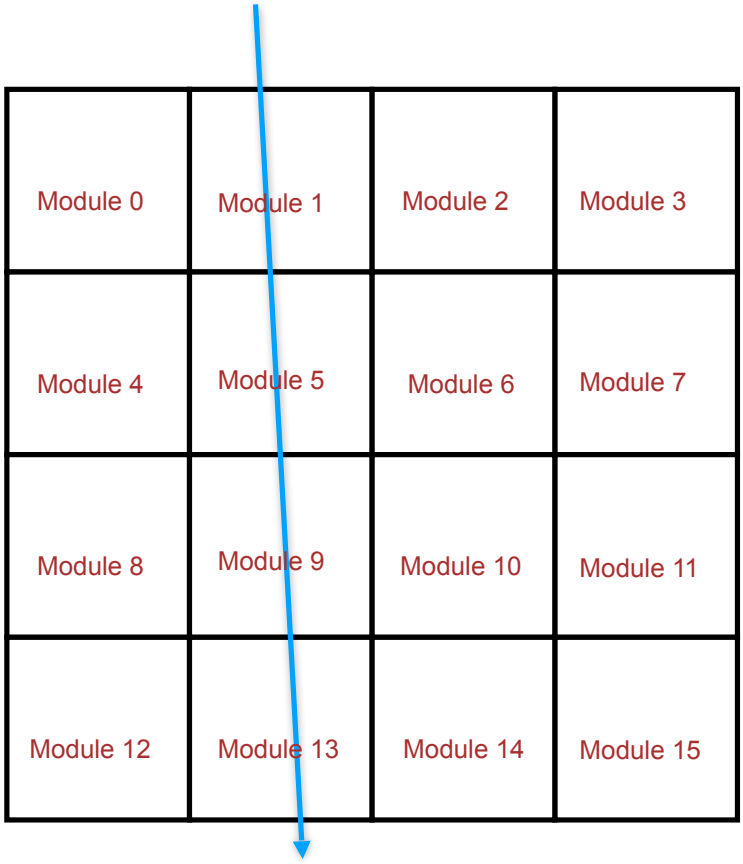

Figure 5.1: 4X4 matrix of tested modules and example of "good event", so of a vertical path.

This trigger consists of a plastic scintillator placed on top of the detector, Fig.5.3; when particles from cosmic rays pass through this scintillator a trigger is formed and each of the individual detector modules' fADCs and TDCs each read out. Cosmic rays are useful for calibrating detector settings like the high voltage settings as they are a constant presence with

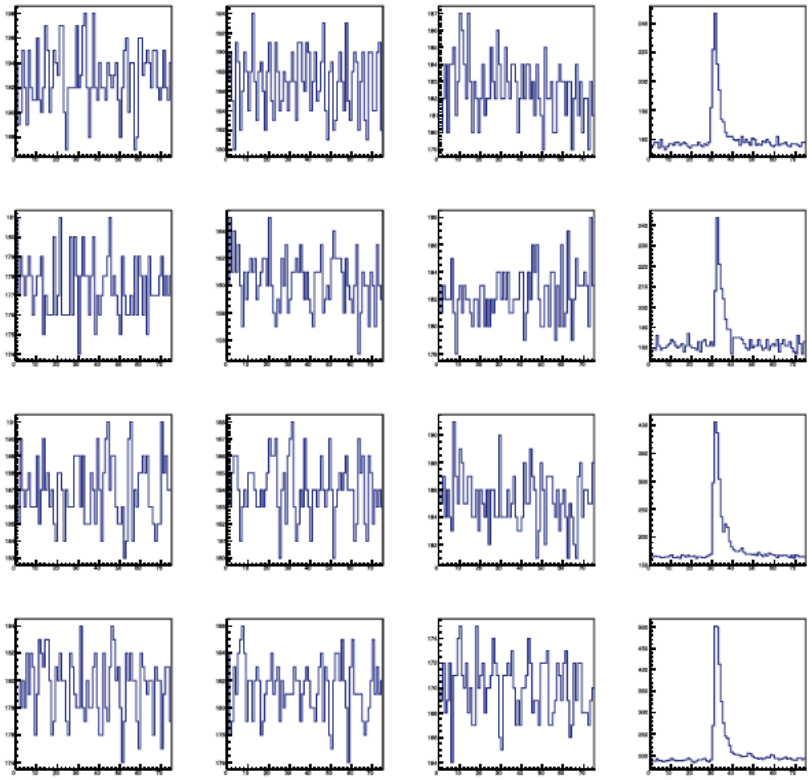

Figure 5.2: Event display: vertical path (3, 7, 11, 15); in the x axis there is the ADC channel, in the y axis there are the counts. Here the inverted PMT signal, as sampled by the FADC, are shown.

a consistent spectrum that can be measured when the electron beam is unavailable.

At the beginning of our test, we put on the HV for each HCAL-J module to test, and we checked the value of HV that gave us a current value about 600 - 615 μA; we found HV values between 1380 and 1400 Volt for each PMT. This operation was useful to verify if all the modules, the electronics and the connections were working good.

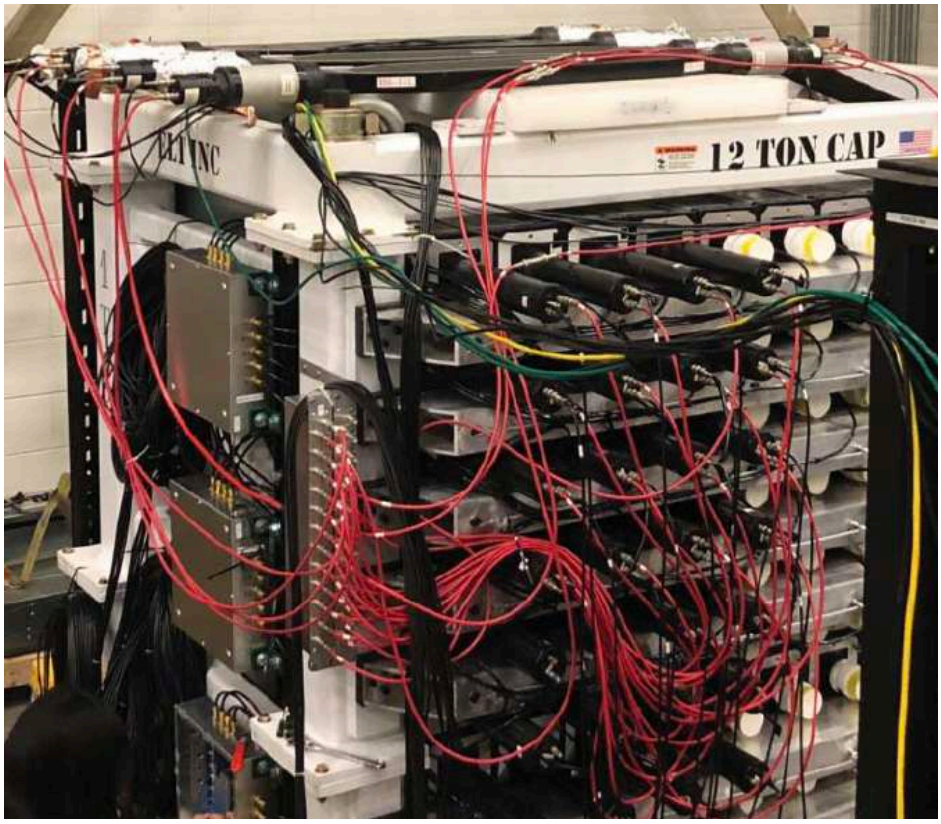

Figure 5.3: 4×4matrix of HCAL-J modules with HV cables connections (in red), signal cable connections (in black) and four paddles on the top to give the trigger.

We analysed the response of each ADC channel: as an example we show the typical spectra for modules number 5 and 9, when imposing the quadruple coincidence for the vertical path identified by the modules 1, 5, 9 and 13, Fig. 5.4. Four vertical modules traversed by the same cosmic are considered a "good event" 5.1.

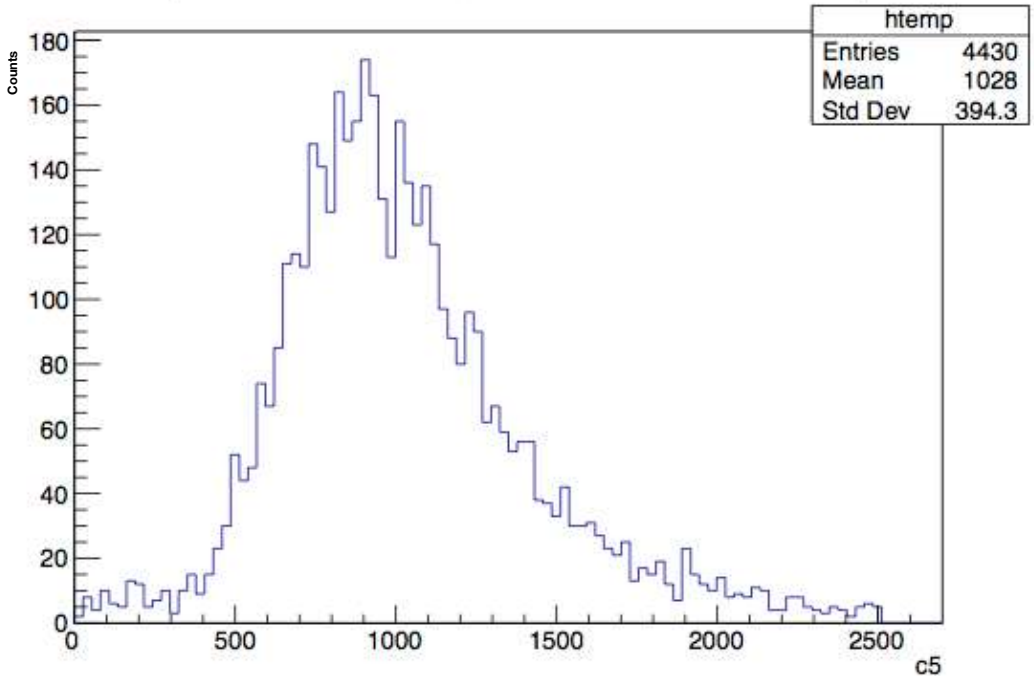

Figure 5.4: ADC Spectrum for module n°5; we have selected events on the vertical path (modules 1, 5, 9, 13).

PMTs gain

We studied the gain of the PMT's when changing the value of the HV, to construct the gain curve; we found the following results:, Fig. 5.5, Tab. 5.1, where A_1 and A_2 are respectively the largest and the smallest amplitude taken on all channels, μ is the average and σ the average error, calculated using:

$$\sigma = \sqrt{(A_1 - \mu)^2 + (A_2 - \mu)^2} \tag{5.1}$$

This is only a preliminary study of the PMTs gain, in fact the gain curve study will be completed in the next section, when we will study all the

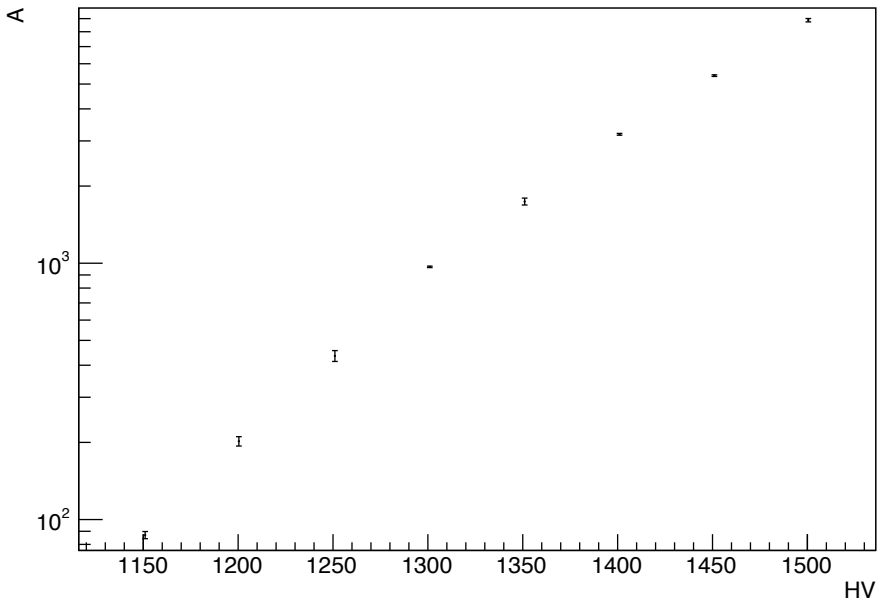

Figure 5.5: Trend of the amplitude when we change HV, for module number 5.

HV	A_1	A_2	μ	σ
1151 V	89 $\pm$3	85 $\pm$6	87	2.8
1201 V	208 $\pm$5	195 $\pm$4	201	8.5
1251 V	450 $\pm$8	420 $\pm$10	435	21,2
1301 V	953 $\pm$16	984 $\pm$17	968	6,36
1351 V	1704 $\pm$26	1779 $\pm$27	1741	53,7
1401 V	3166 $\pm$56	3202 $\pm$46	3184	25,5
1451 V	5421 $\pm$96	5365 $\pm$106	5393	39,6
1501 V	8772 $\pm$152	8962 $\pm$135	8867	134,3

Table 5.1: Evaluated gain for each PMT, by changing the HV value.

HCAL-J modules.

NPE Study

We also studied the number of photo-electrons from two different cosmic runs; the study is for the PMT number 5 (PMT-190206) because it is in the central part of the studied matrix.
The photo-electron peak is useful to calibrate the PMTs and to evaluate its gain; in particular with the photo-electron peak spectrum, that show us the charge distribution outgoing from the PMT when in the first dynode we have only one electron, we can value the absolute gain of the PMT. For this analysis I used two different runs: number 200 and number 202.

- Run 200: Channel 5 at 1501 Volt.
  We evaluated the peak position of the pedestal, that we have to subtract before the npe calculation, the peak position of the signal and the photo-electron peak position too 5.6.
  The ADC channel of photo-electron peak is 196,7;
  The ADC channel of the signal peak is 10976,2;
  So we can calculate, for PMT number 5, that the number of photo-electron is: $NPE = \frac{Q_{signal}}{Q_{1pe}} = 56$.

- Run 202: Channel 5 at 1601 Volt.
  The same study carried out on the previous run gave the following results: The ADC channel of photo-electron peak is 526,1;
  The ADC channel of the signal peak is 36795,4;
  So we can calculate, for PMT number 5, that the number of photo-

electron is: $NPE = \frac{Q_{signal}}{Q_{1pe}} = 70$.

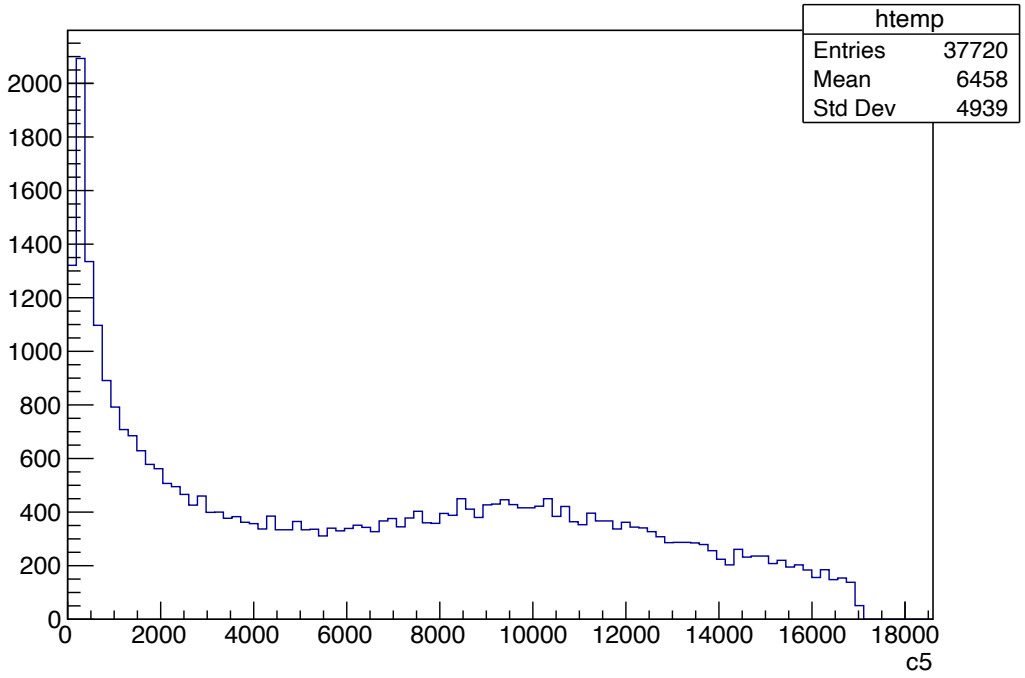

Figure 5.6: Spectrum of channel 5 in which we can see the 3 peaks together: pedestal, single photo-electron peak and signal peak.

These results are in reasonable agreement with the simulation prediction of 72-77 Photo-electrons; a further factor is that, during the tests, the PMTs were not greased but the addition of grease has been found to increase the number of Photo-electrons by as much as 30%.

Timing resolution preliminary study

This test was only a preliminary study, useful to evaluate the HCAL-J modules and to prepare the environment before the complete test; this is

the reason why we used only the fADC to evaluate the timing and not a TDC, which was difficult to find at the test lab in time of the test. We estimated, for module number 5, a timing resolution of 1.8 ns from 15 cm track in module, Fig.5.7; if we subtract the jitter value, Fig.5.8, due to the trigger paddle on the top of HCAL-J, using the following formula:

$$\tau = \sqrt{(\sigma_{CH5})^2 - (\sigma_{Jitter})^2} \tag{5.2}$$

we obtain a timing resolution of 1.48 ns in 15 cm of module.
We have to consider that each ADC channel, in x axis, correspond to 4ns and we are considering only the vertical track, so only the cosmic that crosses the considered module and the other 3 in the same vertical path. A timing resolution of 1.48 ns, is not a good value, considering that from G4SBS simulation we found a value about 0.6 ns, but it is a good point to start our cosmics analysis.

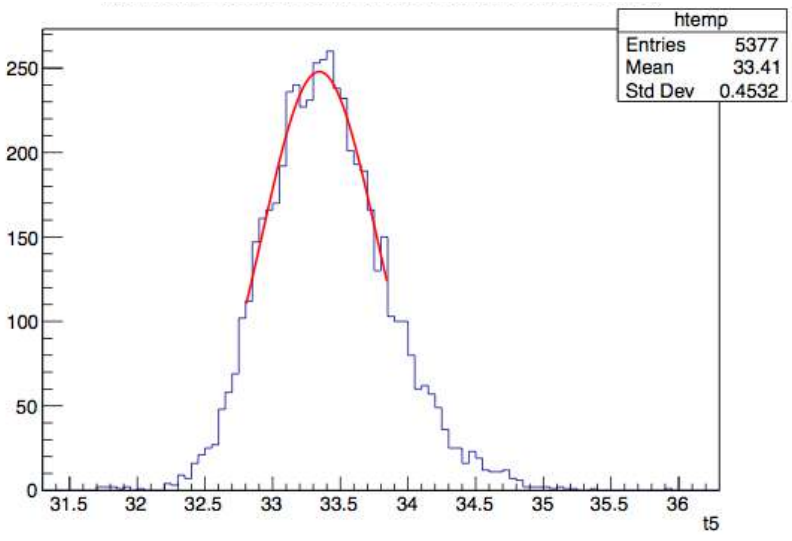

Figure 5.7: Timing Spectrum of channel 5.

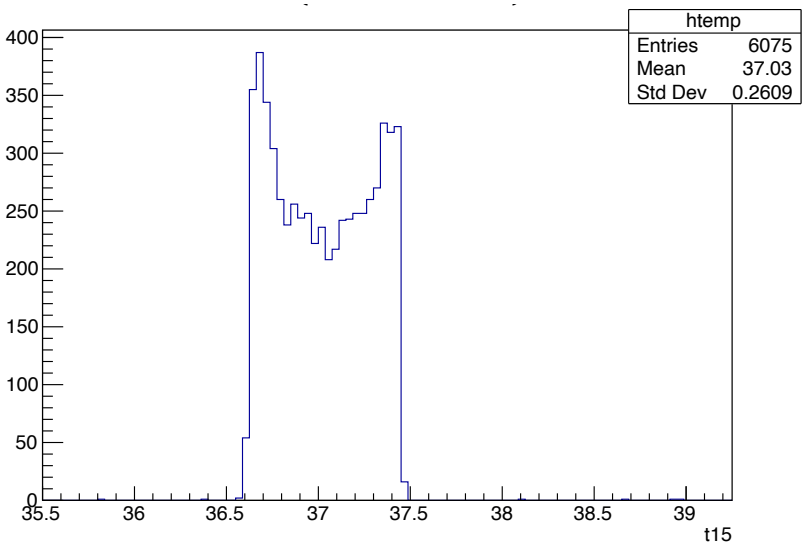

Figure 5.8: Jitter signal

5.2 HCAL-J HV Calibration for 288 modules

During the 2019 the cabling of HCAL-J was completed and during the 2020 new tests started on the Test-Lab.
The first studies were carried out for the calibration of all the modules of the calorimeter, both with cosmics and through LEDs, and to preliminarily study the timing resolution of the calorimeter.

5.2.1 Cosmic Calibration

To calculate the gain curve of the HCAL-J modules, we separately studied the left and the right parts of the calorimeter, using different Cosmic runs. The gain curve is useful to understand if the modules behavior is correct and to find the right HV compromise between gain and PMT s safety.

In Fig. 5.9, a typical cosmic distribution in a single HCAL-J module; the distribution is approximate by a Landau distribution, not a Gaussian one.

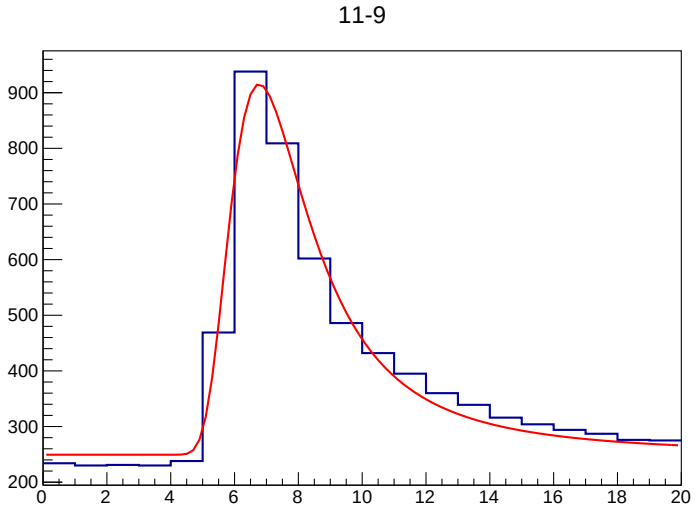

Figure 5.9: Landau fit of a Cosmic distribution in a HCAL-J module.

It is important to underline that we studied the different parts because at Test Lab the calorimeter was divided in two large submatrixes of 12x12 modules each.

Right HCAL-J Part

The modules are numbered from 0 to 143. Following a table, Table 5.2 , with the high voltage used during the different runs; we did 7 different Cosmic runs at different HV values, as we can look in the Table 5.2.
The gain curve, HV vs Amplitude, for each module has a trend as Fig. 5.10 and it follows the function $P_0 * (HV - P_1)^{P_2} - P_3)$ where P_0 is the

Run Number	CMU PMTs Voltage	JLAB PMTs Voltage
1162	-1500 V	-1600 V
1163	-1550 V	-1650 V
1165	-1700 V	-1800 V
1166	-1650 V	-1750 V
1167	-1600 V	-1700 V
1168	-1525 V	-16245 V
1169	-1675 V	-1850 V

Table 5.2: HV values for different Cosmic runs, right part.

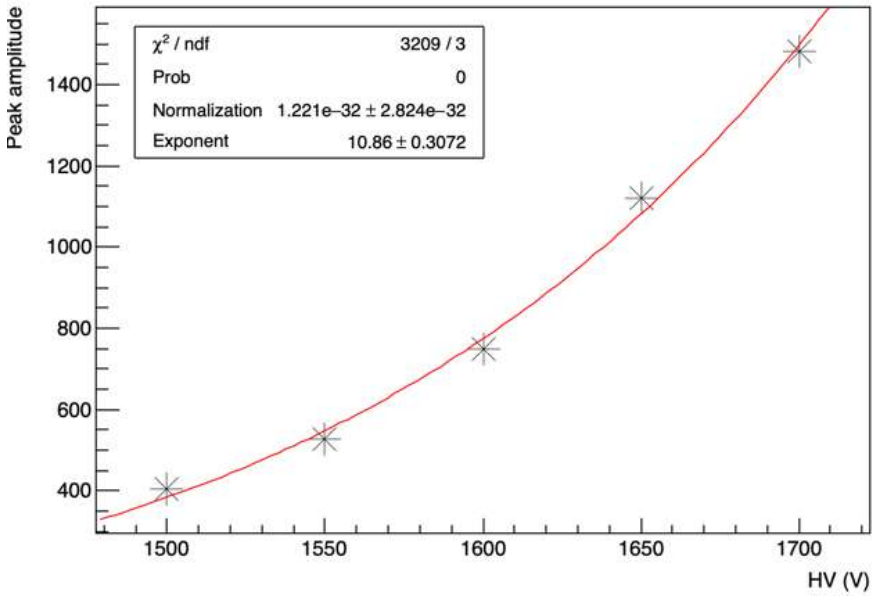

Figure 5.10: Gain curve of module number 110.

normalization, P_1 the X offset, P_2 the exponent and P_3 the Y offset; this function is optimal for the CMU PMTs but not too much for the JLAB's one, so we are looking for an other function that fits better all the PMTs.

Left HCAL-J Part

The modules are numbered from 144 to 287. Following a table, Table 5.3, with the high voltage used during the different runs; we did 7 different Cosmic runs at different HV values, as we can look in the Table 5.3.

Run Number	CMU PMTs Voltage	JLAB PMTs Voltage
978	-1600 V	-1700 V
980	-1700 V	-1800 V
981	-1800 V	-1900 V
984	-1750 V	-1850 V
987	-1650 V	-1750 V
988	-1550 V	-1650 V
989	-1500 V	-1600 V

Table 5.3: HV values for different Cosmic runs, left part.

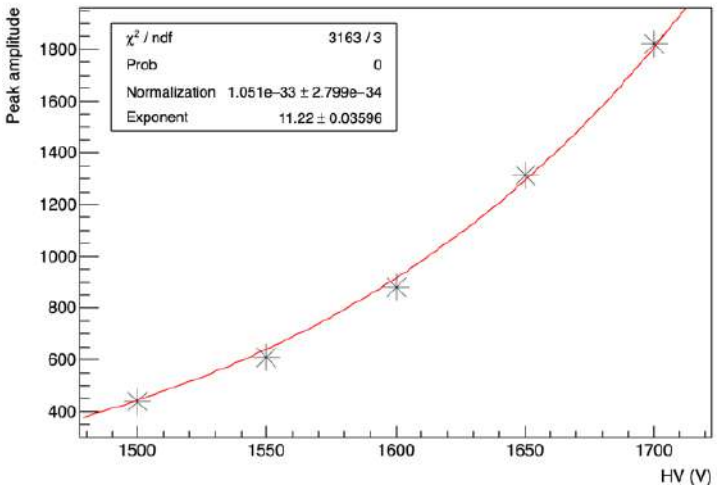

Figure 5.11: Gain curve of module number 248.

Obviously, the fit function is the same used on the right side of the calorimeter. The missing HV points corresponds to those of FADC saturation.

5.2.2 LED Calibration

HCAL-J has a series of 6 LEDS that can illuminate each PMT; each subsequent LED lights up twice as much as the previous one.
We use LEDs for the test because they give us a fast and stable signal to work.
The LED cycle is programmable so we start from LED 0 to LED 5 and every 1000 events it passes to the next led; the first 1000 events, which come from led 0 that means LEDs off,are used to calculate the pedestal for each module. The pedestal histogram is fitted with a Gaussian function, Fig.5.12, and subtracted for each event.

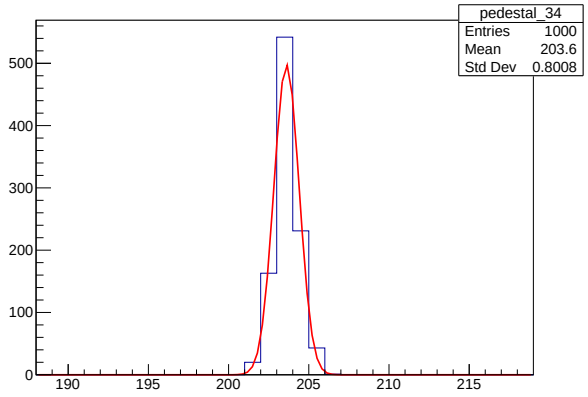

Figure 5.12: Pedestal of pmt number 34; in x axis the unit is RAU (Raw ADC Units) .

For LED calibration we did 12 different runs for each HCAL-J part, Tables 5.55.4; each run consists of about 5000 LED event, thousand for each led. It is important to emphasize that in our runs we didn't cycle through 5 LEDs for every voltage setting; as fADCs started to saturate we switched off LEDs to protect the PMTs, so at the higher voltages we simply cycled between LED0 and LED1, Fig. 5.13; the FADC saturation is due to 4096 RAU (pmt) * 0.75 (electronics)= 61 RAU.

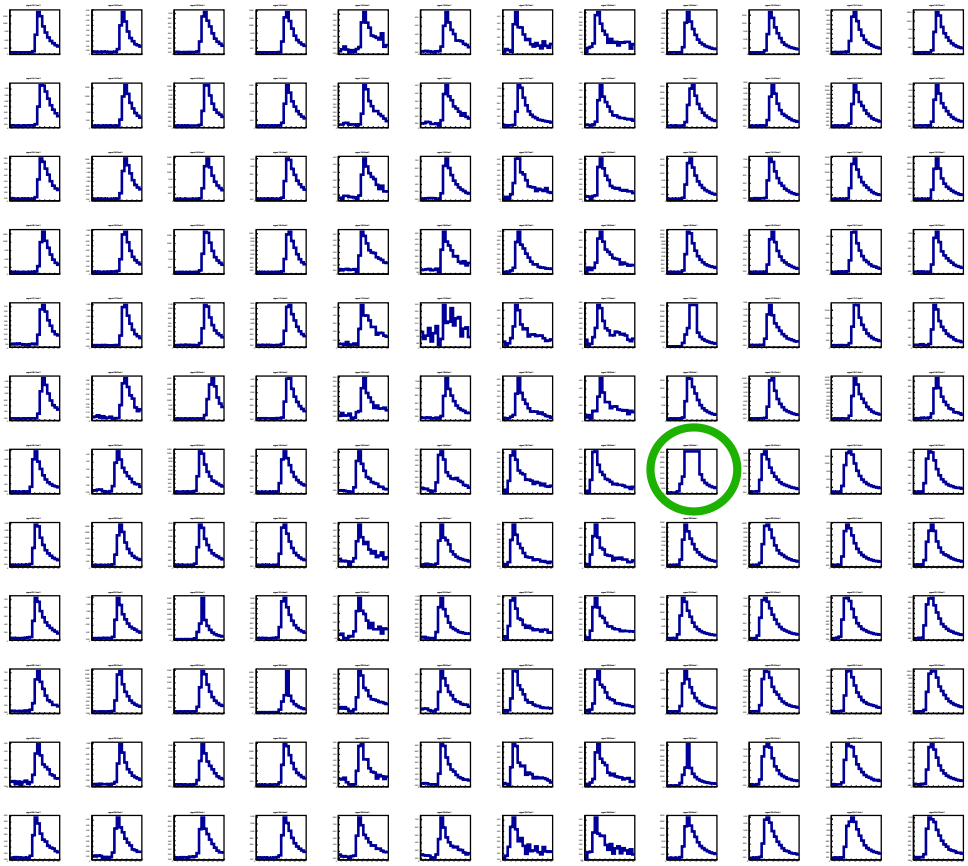

Figure 5.13: FADC response for 144 HCAL-J modules; in green circle we can look a saturated PMT.

After pedestal subtraction, the integrated FADC value spectrum (SRAU= summed raw ADC value) for each led and run was created.
These sRAU histograms are used to create the plot showing srAU vs HV, so the gain curve for each PMT and each LED.

Right HCAL-J Part, gain curve

The modules are numbered from 0 to 143. Following a table, Table 5.4 , with the high voltage used during the different runs.

As for the Cosmic runs, the gain curve for the different LEDs, HV vs

Run Number	CMU PMTs Voltage	JLAB PMTs Voltage
1698	-1675 V	-2050 V
1696	-1625 V	-1950 V
1695	-1600 V	-1900 V
1694	-1575 V	-1850 V
1693	-1550 V	-1800 V
1692	-1525 V	-1750 V
1691	-1500 V	-1700 V
1689	-1475 V	-1650 V
1688	-1450 V	-1600 V
1687	-1425 V	-1550 V
1686	-1400 V	-1500 V
1685	-1350 V	-1450 V

Table 5.4: HV values for different LEDs runs, right part.

Amplitude, for each module has a trend as Fig. 5.14 and it follows the

function $P_0 * (HV - P_1)^{P_2} - P_3)$ where P_0 is the normalization, P_1 the X offset, P_2 the exponent and P_3 the Y offset.

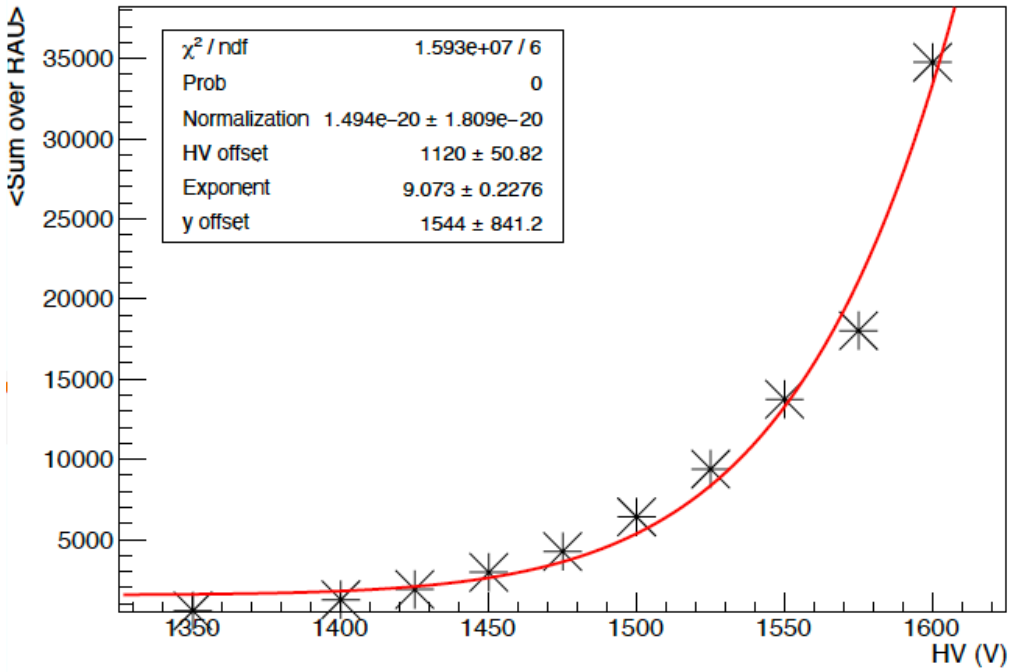

Figure 5.14: LED calibration for a CMU PMTs of HCAL-J.

Left HCAL-J Part, gain curve

The modules are numbered from 144 to 287. Following a table, Table 5.5, with the high voltage used during the different runs.

The fit function, also in this case, is the same, and it is a good approximation for our data, but not the best one; we are still studying new functions to have a very good fit for all PMTs.

Run Number	CMU PMTs Voltage	JLAB PMTs Voltage
1303	-1675 V	-2050 V
1301	-1625 V	-1950 V
1300	-1600 V	-1900 V
1297	-1575 V	-1850 V
1294	-1550 V	-1800 V
1293	-1525 V	-1750 V
1292	-1500 V	-1700 V
1291	-1475 V	-1650 V
1290	-1450 V	-1600 V
1289	-1425 V	-1550 V
1288	-1400 V	-1500 V
1286	-1350 V	-1450 V

Table 5.5: HV values for different LEDs runs, left part.

Number of Photo-electrons

We also evaluated, using the same LED runs of the gain curve analysis, the number of photo-electrons for each LED and each PMTs when the HV changes; it is important to specify that the NPE is not correlated with the HV, but we used this study to find the plateau region to find the good compromise between HV and PE gain, for each HCAL's module.
We can observe the NPE plot for each LED in Fig. 5.16. As you can see, the point number decreases as the LED considered increases; this happens because gradually the brightness becomes bigger and bigger and the FADC saturates at too high voltages.

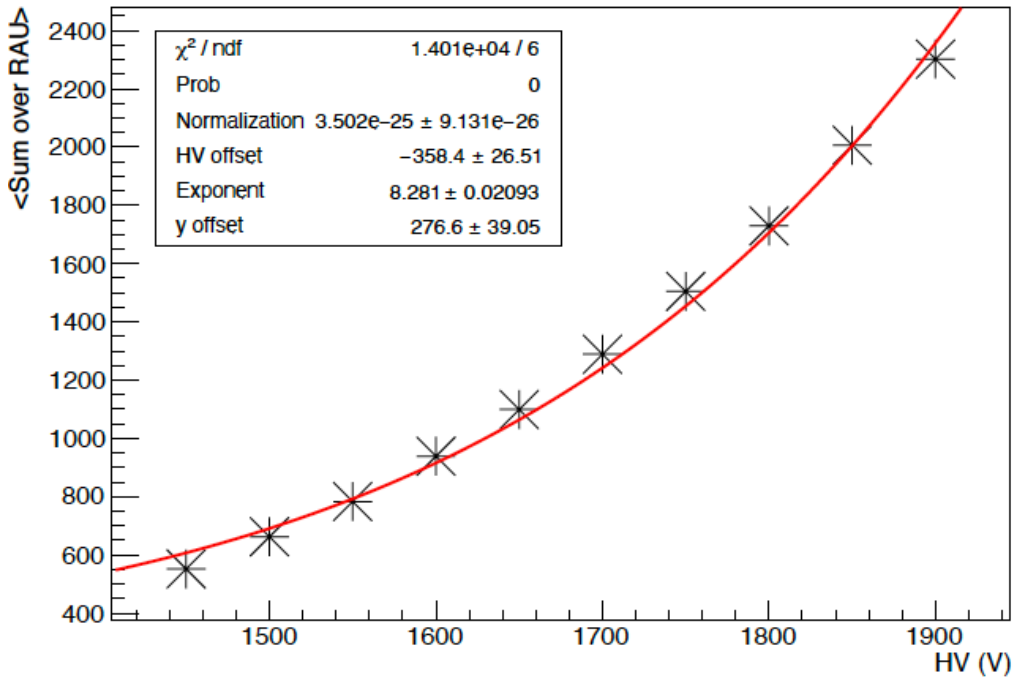

Figure 5.15: LED calibration for a JLAB PMT of HCAL-J.

5.2.3 Summary of HCAL-J modules calibration

Using the calibration results, both from cosmics, LEDs and NPE, we are able to establish the preliminary HV range, for each module, to use during the other test and during the different experiments, Fig. 5.17. These voltage values will certainly be modified in response to the new test that will soon begin in the experimental room, but they are still a fundamental starting point for not overloading the PMTs.

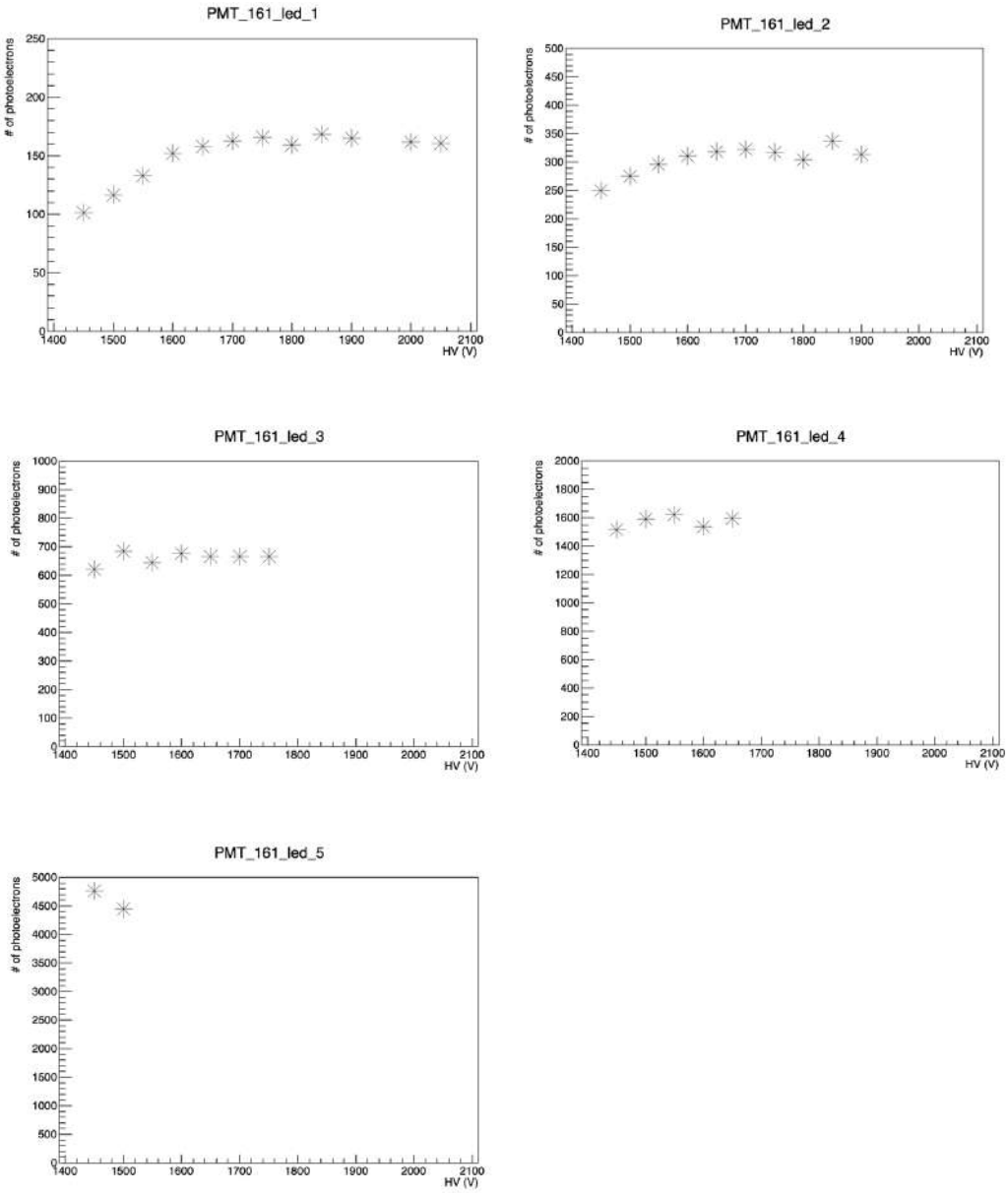

Figure 5.16: NPE for module number 161, when the LED increases.

PMT NUMBER	Recommended HV [Volt]	PMT NUMBER	Recommended HV [Volt]	PMT NUMBER	Recommended HV [Volt]	PMT NUMBER	Recommended HV [Volt]	PMT NUMBER	Recommended HV [Volt]	PMT NUMBER	Recommended HV [Volt]
0	-1450	49	-1475	98	-1475	147	-1500	196	-1750	245	-1550
1	-1475	50	-1525	99	-1525	148	-1750	197	-1625	246	-1750
2	-1550	51	-1525	100	-1750	149	-1750	198	-1750	247	-1750
3	-1500	52	-1750	101	-1550	150	-1750	199	-1750	248	-1500
4	-1750	53	-1625	102	-1750	151	-1750	200	-1450	249	-1525
5	-1750	54	-1750	103	-1750	152	-1475	201	-1525	250	-1525
6	-1750	55	-1750	104	-1500	153	-1500	202	-1475	251	-1525
7	-1750	56	-1450	105	-1525	154	-1525	203	-1525	252	-1525
8	-1475	57	-1525	106	-1525	155	-1525	204	-1500	253	-1500
9	-1500	58	-1475	107	-1525	156	-1475	205	-1525	254	-1475
10	-1525	59	-1525	108	-1525	157	-1475	206	-1450	255	-1475
11	-1525	60	-1500	109	-1500	158	-1475	207	-1525	256	-1750
12	-1475	61	-1525	110	-1475	159	-1525	208	-1750	257	-1750
13	-1475	62	-1450	111	-1475	160	-1750	209	-1700	258	-1750
14	-1475	63	-1525	112	-1750	161	-1750	210	-1750	259	-1750
15	-1525	64	-1750	113	-1750	162	-1700	211	-1600	260	-1525
16	-1750	65	-1700	114	-1750	163	-1750	212	-1450	261	-1525
17	-1750	66	-1750	115	-1750	164	-1475	213	-1525	262	-1525
18	-1700	67	-1600	116	-1525	165	-1525	214	-1500	263	-1525
19	-1750	68	-1450	117	-1525	166	-1475	215	-1525	264	-1525
20	-1475	69	-1525	118	-1525	167	-1525	216	-1525	265	-1525
21	-1525	70	-1500	119	-1525	168	-1525	217	-1525	266	-1500
22	-1475	71	-1525	120	-1525	169	-1500	218	-1500	267	-1475
23	-1525	72	-1525	121	-1525	170	-1475	219	-1475	268	-1750
24	-1525	73	-1525	122	-1500	171	-1525	220	-1750	269	-1650
25	-1500	74	-1500	123	-1475	172	-1750	221	-1750	270	-1750
26	-1475	75	-1475	124	-1750	173	-1750	222	-1750	271	-1750
27	-1525	76	-1750	125	-1650	174	-1750	223	-1750	272	-1500
28	-1750	77	-1750	126	-1750	175	-1750	224	-1450	273	-1525
29	-1750	78	-1750	127	-1750	176	-1500	225	-1525	274	-1525
30	-1750	79	-1750	128	-1500	177	-1575	226	-1525	275	-1525
31	-1750	80	-1450	129	-1525	178	-1475	227	-1525	276	-1525
32	-1500	81	-1525	130	-1525	179	-1475	228	-1525	277	-1525
33	-1575	82	-1525	131	-1525	180	-1475	229	-1475	278	-1525
34	-1475	83	-1525	132	-1525	181	-1500	230	-1525	279	-1525
35	-1475	84	-1525	133	-1525	182	-1475	231	-1525	280	-1750
36	-1475	85	-1475	134	-1525	183	-1500	232	-1750	281	-1750
37	-1500	86	-1525	135	-1525	184	-1750	233	-1750	282	-1750
38	-1475	87	-1525	136	-1750	185	-1750	234	-1750	283	-1750
39	-1500	88	-1750	137	-1750	186	-1700	235	-1750	284	-1500
40	-1750	89	-1750	138	-1750	187	-1750	236	-1525	285	-1525
41	-1750	90	-1750	139	-1750	188	-1500	237	-1525	286	-1525
42	-1700	91	-1750	140	-1500	189	-1525	238	-1525	287	-1525
43	-1750	92	-1525	141	-1525	190	-1525	239	-1525		
44	-1500	93	-1525	142	-1525	191	-1525	240	-1525		
45	-1525	94	-1525	143	-1525	192	-1500	241	-1525		
46	-1525	95	-1525	144	-1475	193	-1475	242	-1475		
47	-1525	96	-1525	145	-1475	194	-1525	243	-1525		
48	-1500	97	-1525	146	-1525	195	-1525	244	-1750		

Figure 5.17: HV recommended values for each PMTs.

5.3 HCAL-J Timing Resolution Preliminary Results

New runs to evaluate the time resolution of the calorimeter were done during the 2020; during these cosmic runs both FADC and TDC was used.

The results come from all HCAL-J, so from a 12x24 matrix.

To calculate the Timing resolution of a specific module, it is necessary that 3 other phototubes in vertical coincidence are fired and that 6 surrounding ones are not fired.

An example of preliminary results is in Fig 5.18.

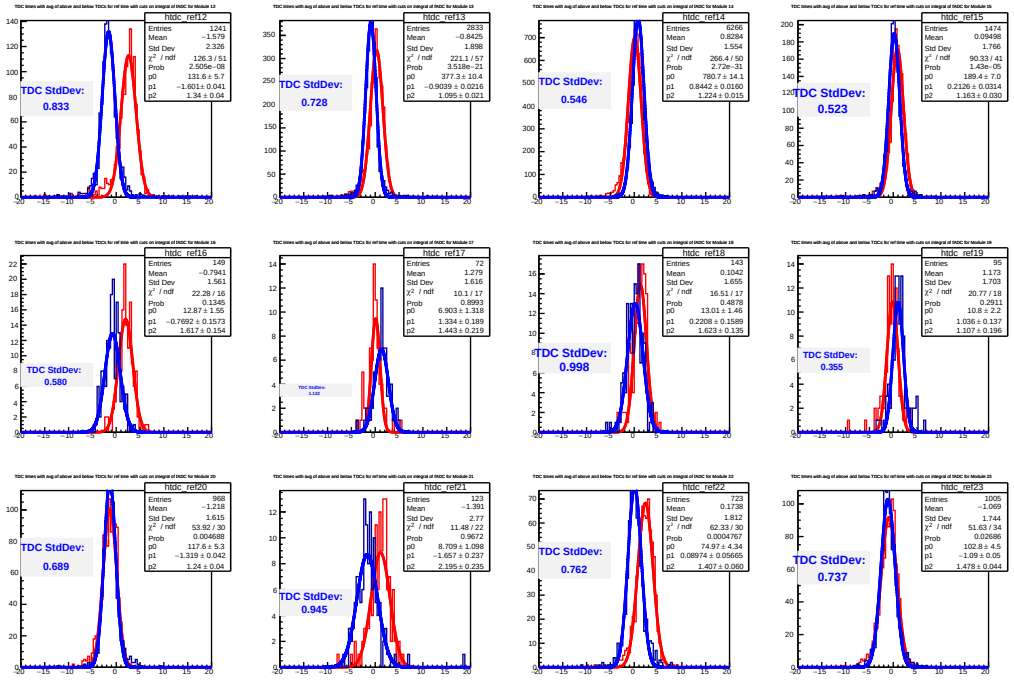

Figure 5.18: TDC timing resolution, for some HCAL-J modules.

Red curve = TDC time – TDC reference, Blue curve = Reference resolution (Top TDC - Bottom TDC).

The TDCs timing resolution changes from 0.4 ns to 1 ns, but could be improved by using the FADC timing resolution together as well.

Conclusions

In this thesis work we discussed the new Super BigBite Spectrometer for the study of the Nucleon's Form Factor, focusing on two of its key detectors: the Triple GEM Front Tracker and the hadronic calorimeter HCAL-J. In summary, we evaluated the Triple GEM response through a series of dedicated simulations, and we characterized HCAL-J parameters performing different tests with Cosmics and LEDs.

As for the Triple GEM, we implemented the avalanche physics simulator based on the GARFIELD++ library and used the finite element ANSYS (and GMSH+ELMER) as mechanical and electrostatic modeler.

A systematic study in terms of amount of charge deposited on the readout plane, arrival time, electron energy and spatial distribution of the electron avalanche on the readout plane, was carried on for a preliminary validation of the simulations models and selection of the most appropriate approach; all simulations were carried on using, as primary particles, electrons and protons of typical energies and incidence angles expected in the SBS experiments. Spatial and temporal distributions as well as rel-

ative gains between electrons and protons obtained from the simulation are qualitatively and quantitatively consistent with expectation, within about 25 % (for gains).

In addiction, we started to reproduced through simulations the experimental conditions of four GEM modules tested at the Juelich/COSY accelerators in the past years. Analyzing the simulations results it was possible to extract the value of the relative gain of the modules, i.e. the number of electrons produced for single event (primary particle) with respect to the number of electrons produced, in a reference GEM module; the relative gain values obtained through the simulations, constitutes a first estimate in agreement with those obtained in the experimental tests of the same module. Comparing the simulations curves and the tests curve we found that the relative gain, are quantitatively consistent within about 25 % for all modules except for one module expected to have an intermediate gain whose systematic deviation from simulation prediction is around 50 %. This anomalous result has been interpreted as a possible misconfiguration or defect of the GEM module, which in fact failed to pass the quality tests during the pre-installation checks. In this respect the implemented GARFIELD++ simulations may have a predictive value, although the considered statistics is very limited. The implemented GARFIELD++ simulation requires a large amount of computational resource which makes almost impossible near-real time comparison with experimental data. Recent developments on the GARFIELD++ library toward a better mesh node search and increased level of parallelism seem to significantly reduce the running time. This improvement will likely

permit a deeper validation of the simulation with the existing test data and the exploitation of its predictions with the commissioning data that is going to be taken in late Summer and early Fall 2021.

As for the Hadronic Calorimeter HCAL-J, the work focused on cabling and components tests as they were completed; in particular we have gradually tested increasingly large matrices of modules starting from 4x4, then 4x6, 6x6, 12x12 and finally 12x24.
The first analysis was based on PMTs behavior and to understand the proper operation of cables, electronics and modules; the first analysis of timing resolution gave us inadequate results, which required to improve the matching between optics and PMTs, using appropriate grease.
From the numerous characterization and calibration tests by Cosmic Rays and by LEDs, it was possible to construct the gain curve of each PMT in order to know the right voltage range to be given to each photomultiplier, to obtain a good performance without risking breaking it. The number of photoelectrons and the range where this number is stable, was also studied and exploited for the determination and improvement of a stable applicable High Voltage interval.
Finally, the temporal resolution of the modules was preliminarily studied using a TDCs based setup; a value between 0.4 ns to 1 ns was found. This resolution is in line with what was expected, but it can also be improved using the resolution coming from the Fast-ADCs modules available in the acquisition chain.
Now, HCAL-J is in hall A, and numerous other tests will be carried out

before its first running in the GMn experiment, starting Fall 2021

Bibliography

[1] McAllister and Hofstadter, Phys. Rev. **102**, 851 (1956).

[2] E.Segrè, *Nuclei e Particelle* (Zanichelli, Collana di Fisica, 1982), Vol. Seconda edizione.

[3] C. Scholz B. Povh, K. Rith, *Particelle e Nuclei* (Bollati Boringhieri, Torino, Italy, 1998), Vol. Seconda edizione.

[4] Akhiezer et al., Sov. Phys. JETP 6, 588 (1958).

[5] B. Wojtsekhowski et al., International Journal of Modern Physics: Conference Series, World Scientific Publishing Company (March, 18 2014).

[6] E. Cisbani et al., EPJ Web of Conferences **73**, 01008 (2014).

[7] C.F. Perdrisat et al., Progr. Nucl. Part. Phys. 59, 694 (2007) .

[8] G. Cates et al., Phys. Rev. Lett. 106 (2010) 252003 .

[9] E. Santopinto, JPS Conf.Proc. 10 (2016) 010010, arXiv:1512.04896 .

[10] R Pohl et al., Nature **466**, 213 (2010).

[11] JLAB website, https://www.jlab.org.

[12] JLAB science website, CEBAF, https://www.jlab.org/accelerator-science.

[13] JLAB website, http://www.jlab.org/srf-institute.

[14] JLAB 12 GeV upgrde website, SRF at Jlab, http://www.jlab.org/12GeV.

[15] "The Super-Bigbite Spectrometer for Jefferson Lab Hall A" https://userweb.jlab.org/ mahbub/HallA/SBS/SBS CDR_New.pdf, .

[16] Critical Design Review "The Super-Bigbite Spectrometer for Jefferson Lab Hall A", https://userweb.jlab.org/ bogdanw/SBS-CDR/SBS-CDR.pdf, 2009.

[17] BB Hodoscope tech spec, https://hallaweb.jlab.org/wiki/images/f/fb/BB-Hodo-technical-specs.pdf.

[18] Experimental Proposal "Measurement of the Neutron Electromagnetic Form Factor Ratio $\frac{G_E^n}{G_M^n}$ at high Q^2", https://hallaweb.jlab.org/collab/PAC/PAC34/PR-09-016-gen.pdf.

[19] Experimental Proposal "Precision Measurement of the Neutron Magnetic Form Factor up to $Q^2 = 18(GeV/c)^2$ by the Ratio Method", https://hallaweb.jlab.org/collab/PAC/PAC34/PR-09-019-gmn.pdf.

[20] "Large Acceptance Proton Form Factor Ratio Measurements at 13 and 15 $(GeV/c)^2$ using the Recoil Polarization Method " https://www.jlab.org/exp_prog/proposals/07/PR12 07-109.pdf, .

[21] Fabio Sauli, Nuclear Instruments and Methods in Physics Research Section A: Accelerators, Spectrometers, Detectors and Associated Equipment, special Issue in memory of Glenn F. Knoll. **805**, (2016).

[22] E. Cisbani, "SBS Front Tracker GEM", SBS Collaboration meeting, 2017.

[23] P. Spindel, "Contribution to the set up of a Gas Electron Multiplier", Institute Superior Industriel de Bruxelles, 2008/2009.

[24] B. Wojtsekhowski et al., Conceptual Design Report (CDR) for the science and experimental equipment for the 12 GeV Upgrade of CEBAF, Newport News, March, 25, 2005.

[25] V.Desmet, "Study of a GEM tracker of charge particles for the Hall A high luminosity spectrometer at Jefferson Lab", Institute Superior Industriel de Bruxelles, 2010/2011.

[26] M. Poli Lener, "Triple-GEM detectors for the innermost region of the muon apparatus at the LHCb experiment", Universita‘ degli Studi di Roma “Tor Vergata”, 2005.

[27] S. Franchino, "Principi di funzionamento ed alcune applicazioni dei rivelatori GEM", Seminario, Pavia, June, 28, 2006.

[28] V. Bellini, E. Cisbani, M. Capogni, S. Colilli, R. De Leo, R. De Oliveira, V. De Smet, R. Fratoni, S. Frullani, F. Giuliani, M. Gricia, F. Librizzi, M. Lucentini, F. Mammoliti, S. Minutoli, P. Musico, F. Noto, R. Perrino, F. Santavenere, and C. Sutera, Journal Of Instrumentation **7**, (2012).

[29] M. Raymond et al., IEEE Nuclear Science Symposium Conference Record (2000).

[30] V.Brio et al., Radiation Effects and Defects in Solids **173**, 857 (2018).

[31] N. V. Vlasov et al., Instruments and Experimental Techniques **49**, 41 (2006).

[32] S. Barcus et al, *"A Hadron Calorimeter for Nucleon Form Factor Measurements"* (PUBLISHER, ADDRESS, June, 25, 2020).

[33] J. Alcorn et al., Nucl. Instrum. Meth. A **522**, 294 (2004).

[34] W. Watson, J. Chen, G. Heyes, E. Jastrzembski, and D. Quarrie, CODA: A scalable, distributed data acquisition system, in: 8th Real-Time Computer Applications in Nuclear, Particle and Plasma Physics (RT 93), 1993, pp. 296-303. .

[35] A.Puckett, g4SBS - Geant4 simulator in SBS, website, "https://hallaweb.jlab.org/wiki/index.php/Documentation_of_g4sbs".

[36] ANSYS website, http://www.ansys.com.

[37] Garfield web page, https://garfieldpp.web.cern.ch/garfieldpp/.

[38] ROOT web page, https://root.cern.

[39] V Bellini, V Brio, E Cisbani, K Kmieć, L Lagamba, R Perrino, C Petta, L Re, and C Sutera, Journal of Physics: Conference Series **1498**, 012009 (2020).

[40] J ulich COSY accelerator web page, https://www.fz-juelich.de/ikp/EN/Forschung/Beschleuniger/_doc/COSY.html.

[41] L.G. Re, Caratterizzazione del tracciatore GEM per lo spettrometro SBS di JLAB e algoritmi evolutivi di pre-tracciamento, 2016, master thesis, Università degli Studi di Catania.

[42] O. Bouhali 1 Sheharyar 1, a and A. Castaneda 1, EPJ Web Conf. **Volume 174**, (2018).

Acknowledgements

For the realization of this PhD work, I thank my Tutors, Prof. C. Petta, Dr.ssa M.C. Sutera, Dr. E. Cisbani, Prof. V. Bellini, Dr. F. Tortorici, Dr. L.G. Re and the whole JLAB12 group. I also thank B. Wojtsekhowski and the entire American group HCAL-J Working Group.
I sincerely thank my family who have always supported me in my work.